Cell Reports

Article

# Phase separation of TTBK2 and CEP164 is necessary for ciliogenesis

## Graphical abstract

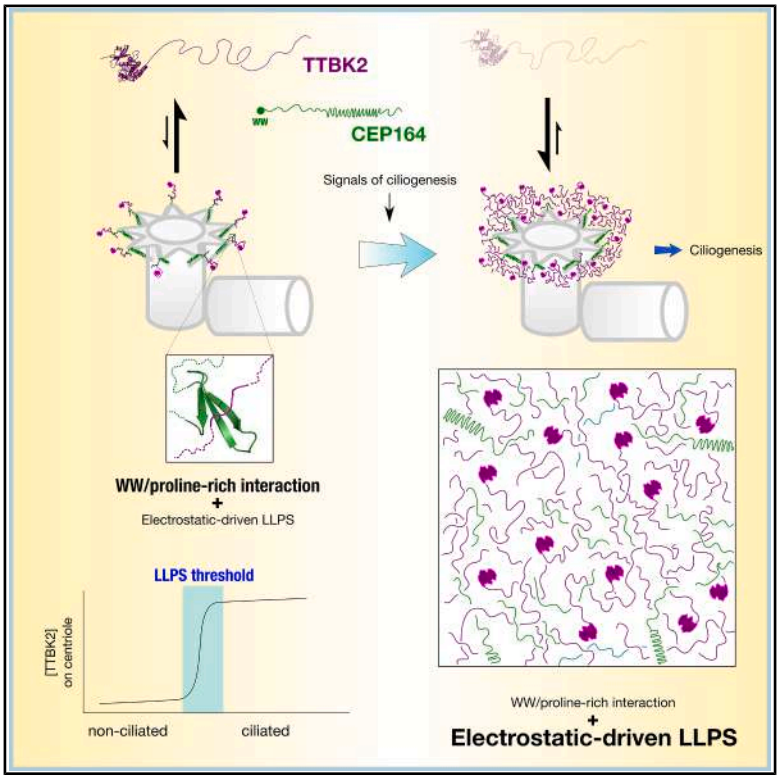


## Highlights

- CEP164 forms dynamic, liquid-like condensates with TTBK2
- Electrostatic interaction drives the phase separation of CEP164 and TTBK2
- Phase separation of TTBK2 and CEP164 enhances TTBK2 recruitment to centrioles
- Phase separation of TTBK2 and CEP164 is essential for efficient ciliogenesis

## Authors

Po-Chun Chou, Yu-Hao Lin, I-Hsuan Lin, ..., Yu-Chun Lin, Jie-rong Huang, Won-Jing Wang

## Correspondence

jierongh@nycu.edu.tw (J.-r.H.), wangwj@nycu.edu.tw (W.-J.W.)

## In brief

Chou et al. demonstrate that CEP164 recruits TTBK2 to centriole distal appendages through phase separation driven by electrostatic interactions between their intrinsically disordered regions. This multivalent interaction forms dynamic condensates, facilitating efficient TTBK2 recruitment and initiating ciliogenesis, highlighting the critical role of phase separation in cilia formation.

Chou et al., 2025, Cell Reports *44*, 115810
June 24, 2025 
https://doi.org/10.1016/j.celrep.2025.115810

CellPress

Cell Reports

CellPress
OPEN ACCESS

Article

# Phase separation of TTBK2 and CEP164 is necessary for ciliogenesis

Po-Chun Chou,[1,2] Yu-Hao Lin,[1,2] I-Hsuan Lin,[1] Tzu-Ying Lin,[3] Yun-Chia Huang,[1] Shi-Rong Hong,[3] Ting-Jui Ben Chang,[4] Yin Fang,[3] Yizhi Lin,[1] T. Tony Yang,[4] Yu-Chun Lin,[3] Jie-rong Huang,[1,2,5,6,*] and Won-Jing Wang[1,2,7,8,*]

[1]Institute of Biochemistry and Molecular Biology, National Yang Ming Chiao Tung University, Taipei 112304, Taiwan
[2]Program in Molecular Medicine, National Yang Ming Chiao Tung University and Academia Sinica, Taipei, Taiwan
[3]Institute of Molecular Medicine, National Tsing-Hua University, Hsinchu 300044, Taiwan
[4]Department of Electrical Engineering, National Taiwan University, Taipei 106319, Taiwan
[5]Institute of Biomedical Informatics, National Yang Ming Chiao Tung University, Taipei 112304, Taiwan
[6]Department of Life Sciences and Institute of Genome Sciences, National Yang Ming Chiao Tung University, Taipei 112304, Taiwan
[7]Advanced Therapeutics Research Center, National Yang Ming Chiao Tung University, Taipei 112304, Taiwan
[8]Lead contact
*Correspondence: jierongh@nycu.edu.tw (J.-r.H.), wangwj@nycu.edu.tw (W.-J.W.)
https://doi.org/10.1016/j.celrep.2025.115810

## SUMMARY

The primary cilium plays a crucial function in sensing and transmitting extracellular signals into cells. The initiation of ciliogenesis hinges on the recruitment of Tau tubulin kinase 2 (TTBK2) to the distal appendages (DAs) of centrioles through CEP164. However, the detailed mechanism underlying the CEP164/TTBK2 interaction at DAs during ciliogenesis remains incompletely understood. In this study, we unveil that CEP164 features a long intrinsically disordered region and forms dynamic condensates with TTBK2 through phase separation. Our investigation demonstrates that CEP164 undergoes phase separation with TTBK2 through multivalent electrostatic interactions. These interactions facilitate the efficient recruitment of TTBK2 to DAs, thereby kickstarting the process of cilia formation. Therefore, our findings provide insights into the molecular regulation of CEP164/TTBK2 interactions at DAs and highlight the pivotal role of phase separation in promoting cilia formation.

## INTRODUCTION

Primary cilia are vital organelles responsible for cells detecting and reacting to signals from the extracellular environment.[1,2] Defects in primary cilia function result in genetic disorders known as "ciliopathies."[3] The assembly of primary cilia follows tightly regulated steps.[4–8] The cilia initiation step requires the presence of a specialized pinwheel-like structure called centriole distal appendages (DAs) that are located at the distal end of the mother centrioles.[9,10] Various proteins, including CEP83, CEP89, SCLT1, CEP164, LRRC45, ANKRD26, and FBF1, have been identified as constituents of DAs.[10–15] CEP83 is the initial DA protein recruited to the centrioles[10,16] and is necessary for recruiting SCLT1 and CEP89. SCLT1, in turn, plays a role in recruiting CEP164 and LRRC45.[10] Finally, LRRC45 takes on the responsibility of recruiting FBF1.[14] By utilizing direct stochastic optical reconstruction microscopy (dSTORM), the detailed localization of those proteins within the DAs has been elucidated. CEP83, SCLT1, and CEP164 are located in the structure backbone of the DAs, with CEP83 positioned at the core and CEP164 situated at the periphery of the pinwheel-like DA structure.[17,18]

After DA formation, Tau tubulin kinase 2 (TTBK2), a pivotal enzyme for initiating ciliogenesis,[19,20] is recruited through its interaction with the CEP164.[11,21,22] TTBK2 binds to CEP164 through its proline-rich C-terminal region, interacting with the WW domain in the N-terminal region of CEP164. Once recruited, TTBK2 phosphorylates several proteins at the centrioles,[23,24] facilitating ciliary vesicle docking and initiating ciliogenesis. The interaction of CEP164 and TTBK2 is critical for ciliogenesis. However, the reported interaction between CEP164's WW domain and TTBK2's proline-rich region is weak (at a micromolar range), and the reported structure was only based on the fused small fragments of the two.[21] This weak interaction may not sufficiently stabilize TTBK2's stays on the centrioles, and thus, the force that recruits TTBK2 and enriches it around the DAs during ciliogenesis remains unclear.

PONDR analysis[25] predicts that CEP164 and TTBK2 both possess extensive intrinsically disordered regions (IDRs), and recently, many studies have highlighted the importance of IDRs in assisting with the assembly of membraneless organelles through a phase separation mechanism.[26,27] This mechanism explains the spatiotemporal controls of many biological reactions, such as gene regulation,[28–31] signal transduction,[32] cell quality control,[33,34] autophagy,[35–37] DNA repair,[38] cell junction,[39,40] and skin barrier formation.[41] In particular, some are also related to centriole functions. For example, the protein SPD-5 undergoes phase separation for scaffolding pericentriolar materials assembly and centrosome duplication.[42] Polo-like kinase 4, a key regulator of centriole duplication, undergoes phase separation to drive centriole biogenesis.[43,44] TTBK2

and CEP164 share structural disorder and sequence features similar to those phase-separated proteins, suggesting possible interaction through this mechanism.

Here, we demonstrate that CEP164 forms dynamic condensates with TTBK2. Our biochemical analysis reveals that CEP164 and TTBK2 undergo phase separation, primarily driven by multivalent electrostatic interactions. Importantly, we find that the phase separation of CEP164 and TTBK2, in conjunction with previously characterized binding between the WW domain of CEP164 and the TTBK2 proline-rich region,[11,21,22] plays a crucial role in regulating TTBK2 recruitment to the centrioles, thereby initiating cilia formation.

## RESULTS

### Cep164 dynamically condenses at the centriole during ciliogenesis

Although CEP164 is known to be an essential component of DAs for primary cilia formation, the precise spatial distribution of CEP164 at DAs during ciliogenesis remains obscure. To elucidate this, we used expansion dSTORM (Ex-dSTORM) to document the single-molecular localization pattern of CEP164 during ciliogenesis. In unsynchronized RPE1 cells, poly-glutamylated tubulin (pGlu-Tu) staining was used to distinguish between ciliated and non-ciliated cells. Axial-view Ex-dSTORM images of endogenous CEP164 showed that the localization of CEP164 at the DAs exhibited a greater proximity to the axoneme in ciliated cells than in non-ciliated cells. This observation suggests a dynamic localization of CEP164 at DAs during ciliogenesis (Figures 1A–1D).

Except for a WW domain positioned at its extreme N terminus, CEP164 lacks well-defined structure domains, as indicated by IDR prediction (Figure 1E). Nevertheless, several coiled-coil segments were also predicted in this region (Figure 1E). This is noteworthy because both coiled-coil segments and IDRs are often associated with driving protein phase separation. The FuzDrop server[45] further supports this notion, indicating a high probability of phase separation occurrence within CEP164 (Figure 1E). To assess whether CEP164 undergoes phase separation, we expressed the FLAG- and hemagglutinin (HA)-tagged CEP164 (FH-CEP164) in U2OS cells. Using centrin as a centriole maker, FH-CEP164 was detected at one of the centrioles (Figure 1F), agreeing with the reported works.[12] Interestingly, we observed that overexpression of FH-CEP164 led to condensate formation at both the mother centrioles and in the cytoplasm (Figure 1F). This phenomenon was not limited to specific epitope tags, as various epitope-tagged CEP164 also induced condensate formation (Figure S1A). We further generated GFP-CEP164 truncation mutants and expressed them in *CEP164* knockout U2OS cells to assess their ability to form condensates (Figures S1B–S1E). The C-terminal fragment of CEP164 (residue number 589–1460; $CEP164^{589E}$), but not the N-terminal fragment of CEP164 (residue number 1–588; $CEP164^{1–588}$), induced condensate formation (Figures S1F and S1G).

To examine the dynamic properties of CEP164 condensates, we expressed GFP-CEP164 in U2OS cells and conducted fluorescence recovery after photobleaching (FRAP) experiments. Following photobleaching, both GFP-CEP164 condensates at the centrioles and those in the cytosol exhibited rapid fluorescence recovery, indicating that CEP164 formed dynamic, liquid-like condensates (Figures 1G, 1H, S1H, and S1I). Time-lapse images further revealed that those condensates underwent fusion and fission events, reinforcing their liquid-like behavior (Figure 1I). To explore the potential differences in CEP164 condensate characteristics between ciliated and non-ciliated cells, we co-expressed GFP-CEP164 and 5HT6-mCherry (a ciliary marker) in 3T3 cells. Cells were serum starved to induce cilia formation. Our FRAP experiments revealed no significant difference in the recovery rates of CEP164 condensates between control and serum-starved cells (Figures 2A and 2B), indicating that the liquid-like properties of CEP164 are preserved at the centrioles regardless of the ciliation status.

To examine whether endogenous CEP164 formed similar dynamic condensates, we applied CRISPR-Cas9-mediated homologous recombination to insert GFP at the N terminus of the *CEP164* locus. Genotyping and western blot analysis confirmed the successful GFP insertion in one *CEP164* allele (Figures 2C and 2D). Immunostaining confirmed that GFP-CEP164 localizes at the DAs and is able to recruit TTBK2 (Figure 2E). FRAP analysis of these GFP-CEP164 condensates demonstrated rapid fluorescence recovery, confirming that endogenous CEP164 exhibits highly dynamic behavior within these condensates (Figures 2F and 2G). Collectively, our findings indicate that CEP164 undergoes phase separation, rather than aggregation, at the centrioles, forming dynamic, liquid-like condensates.

### TTBK2 is recruited to CEP164 condensates in a kinase-independent manner

CEP164 serves as the recruiter of TTBK2 to the mother centriole for cilia initiation.[11,21,22] Here, we stained CEP164 condensates and observed that TTBK2 was detected in the CEP164 condensates (Figure 3A). Although TTBK2 also features a long IDR, we did not observe TTBK2 condensates in the cytoplasm when overexpressing FH-TTBK2 in U2OS cells (Figures S2A and S2B). Because TTBK2 is the critical kinase required for ciliogenesis,[20] we investigated whether its enzyme activity influenced the formation of CEP164 condensates. Here, we generated *TTBK2* knockout U2OS cells and confirmed TTBK2's depletion by genotyping, immunostaining, and immunoblotting (Figures S2C–S2E). Full-length TTKB2 ($TTBK2^{FL}$) and the kinase-dead TTBK2 mutant ($TTBK2^{KD}$) were re-introduced in *TTBK2* knockout U2OS cells (Figure S2E). Since GFP-CEP164 still formed condensates in both $TTBK2^{FL}$- and $TTBK^{KD}$-expressing cells, this indicates that the recruitment of TTBK2 to CEP164 condensates is independent of TTBK2's activity (Figure S2F).

Next, we search the minimum segment for TTBK2's location at CEP164 condensates. We generated different HA-tagged TTBK2 truncations and co-transfected them with Myc-CEP164 (Figure 3B). The construct from residue 1074 to the C-terminal end ($TTBK2^{1074E}$) retained the ability to localize to the CEP164 condensates, whereas the shorter one ($TTBK2^{1085E}$) lost its ability to target CEP164 condensates (Figures 3C, 3D, and S3A). Interestingly, $TTBK^{1074E}$ was also mapped as the minimal region of TTBK2 responsible for its localization at the centrioles, suggesting that the phase separation of CEP164 may regulate the

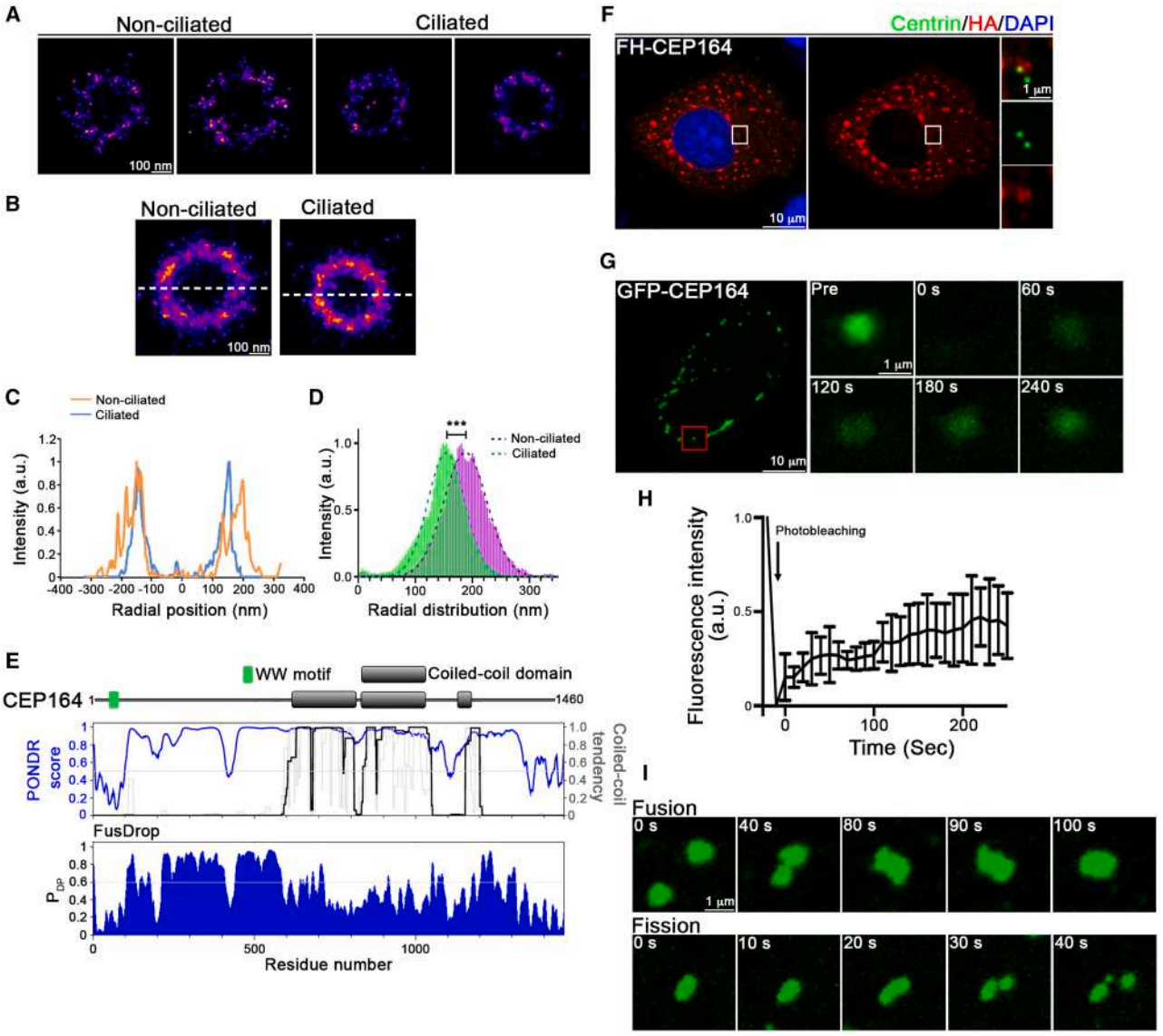


**Figure 1. CEP164 shows phase separation property**

(A) Representative Ex-dSTORM images show endogenous CEP164 patterns in ciliated and non-ciliated RPE1 cells. The localization of CEP164 at DAs was acquired from an axial view. Scale bar, 100 nm.

(B) Averaged images of CEP164 signals indicate its possible localization at ciliated ($n$ = 14) and non-ciliated ($n$ = 16) centrioles. Scale bar, 100 nm.

(C) Intensity profile of CEP164 distribution extracted along the dashed lines for each condition. CEP164 localization at the DAs demonstrated a closer proximity to the axoneme in ciliated cells (blue line) compared to non-ciliated cells (orange line).

(D) The diameter of CEP164 ring at the mother centrioles was measured. The data are presented as mean ± SD. ***$p < 0.0001$ by Student's t test.

(E) The primary sequence of CEP164 was analyzed using PONDR, COILS, and FuzDrop, with residues numbered accordingly. Coiled-coil propensity is indicated by the gray line, while PONDR-predicted disordered regions are marked with the blue line. $P_{DP}$, residue-based droplet-promoting probability.

(F) FH-CEP164 was expressed in U2OS cells followed by centrin and HA staining. DNA was stained with DAPI. Regions within the marked boxes are magnified and shown on the right. Scale bars are as indicated.

(G) GFP-CEP164 was expressed in U2OS cells and subjected to FRAP analysis. The bleached region is marked with the red square, and the magnification of the marked area is presented on the right. The elapsed time after photobleaching and the scale bars are as indicated.

(H) FRAP measurements of GFP-CEP164 at various time points reveal changes in the dynamics of GFP-CEP164 condensates, with the corresponding intensity curve presented as the mean ± SD ($n$ = 7).

(I) GFP-CEP164 condensates underwent fusion and fission events over time. Scale bar, 1 μm.

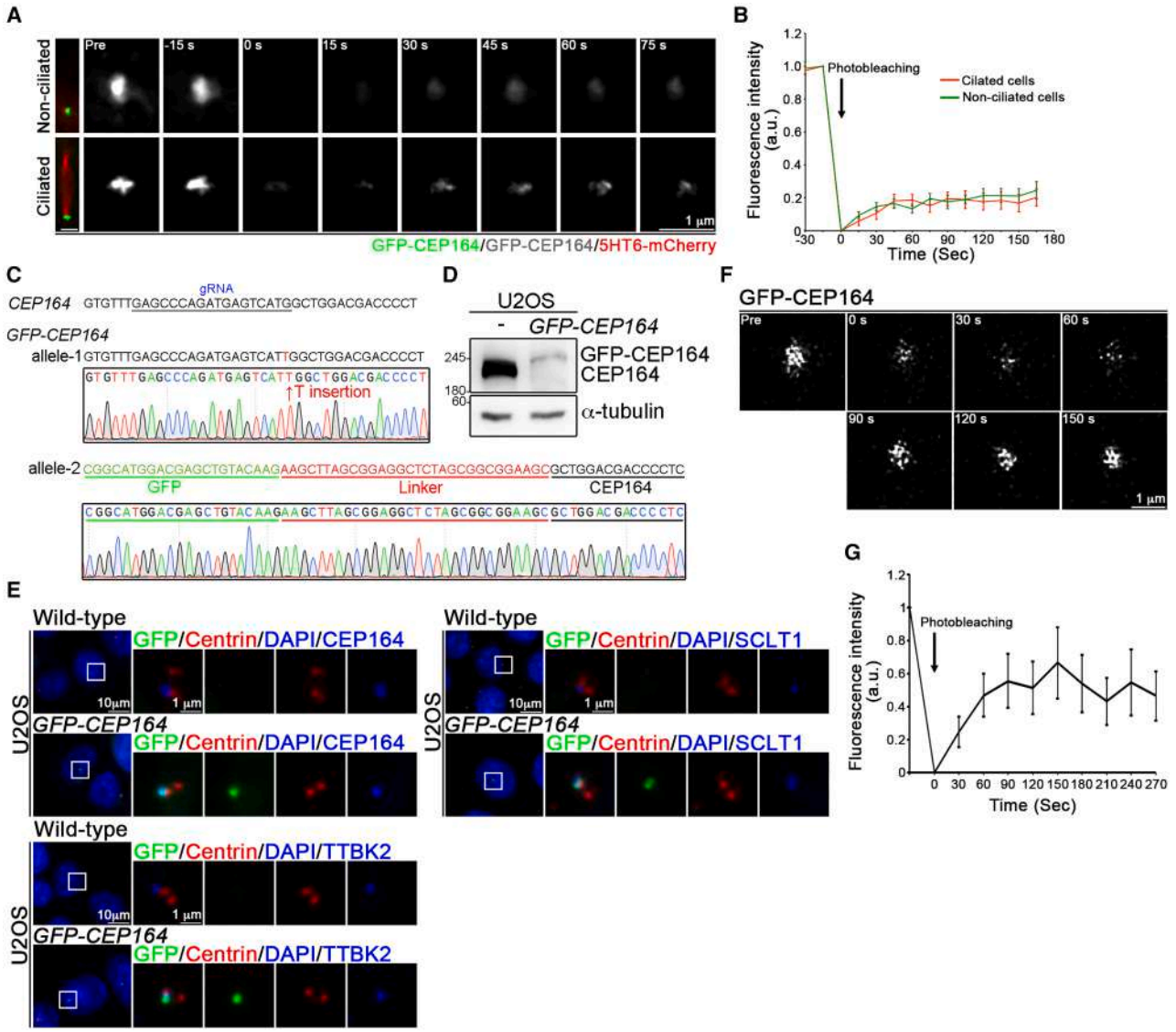


**Figure 2. Endogenous CEP164 shows phase separation property**

(A) NIH3T3 cells were transfected with 5HT6-mCherry (a cilia marker, red) and GFP-CEP164 (green). Transfected cells were incubated with serum-free medium or control medium for 24 h. GFP-CEP164 fluorescence was photobleached and then allowed to recover for the indicated times. Scale bar, 1 μm.

(B) Normalized fluorescence intensity of GFP-CEP164 in ciliated cells (red curve) and non-ciliated cells (green curve). Data represent the mean ± SD. $n$ = 12 (ciliated cells) and 9 (non-ciliated cells) from 3 independent experiments.

(C) GFP was inserted at the N terminus of *CEP164* locus. Genotyping analysis of *CEP164* alleles is shown.

(D) Western blot (WB) analysis was performed in wild-type and *GFP-CEP164* knockin U2OS cells using anti-CEP164 and anti-α-tubulin antibodies.

(E) Immunostaining was performed in wild-type and *GFP-CEP164* knockin U2OS cells using antibodies as indicated. Scale bars are as indicated.

(F) GFP-CEP164 signal was photobleached and then allowed to recover for the indicated times. Scale bar, 1 μm.

(G) Data represent the mean ± SD $n$ = 20 cells from 3 independent experiments..

docking or the enrichment of TTBK2 at the mother centrioles for cilia formation (Figures S3B and S3C).

## TTBK2 and CEP164 interaction promotes condensate formation *in vitro*

In addition to using the minimal segment of TTBK2 to join the condensates, we also confirmed that CEP164$^{1–588}$ was responsible for its interaction with TTBK2 (Figure 3E), agreeing with previous publications.[11,21,22] We thus purified TTBK2$^{1074E}$ and CEP164$^{1–588}$ from bacteria to investigate their interaction mechanism (Figures S4A and S4B). CEP164$^{1–588}$ or TTBK2$^{1074E}$ remained soluble at a concentration of 20 μM in phosphate buffer (10 mM, pH 6.5) (Figures 3F and S4C). Notably, even at a higher concentration of 100 μM or in the presence of a 10% crowding agent, CEP164$^{1–588}$ remained soluble (Figure S4C). However, when we mixed 20 μM CEP164$^{1–588}$ and TTBK2$^{1074E}$

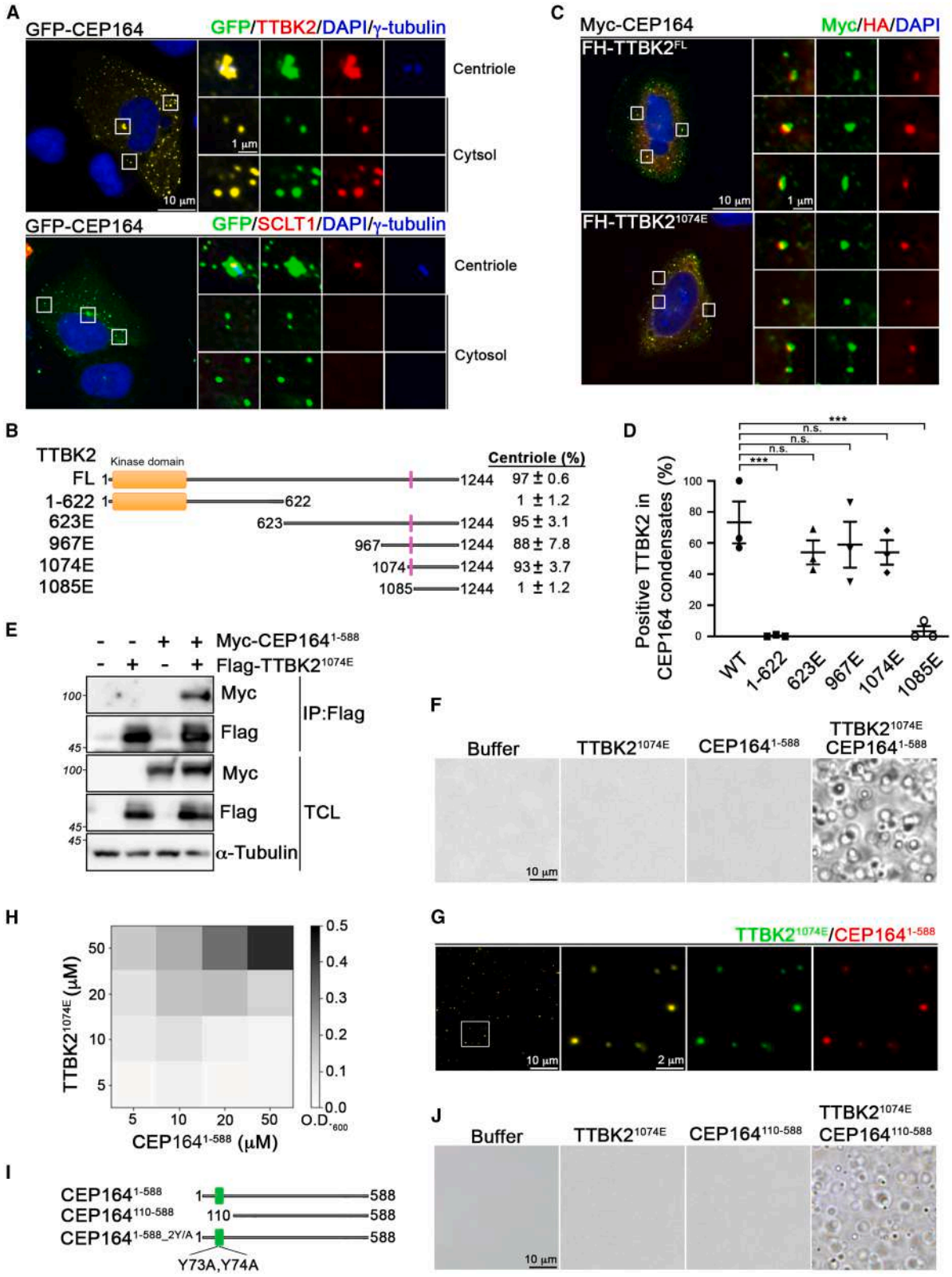


*(legend on next page)*

at a ratio of 1:1, the solution became turbid, suggesting that the interaction between CEP164 and TTBK2 promotes CEP164 condensate formation (Figure 3F). We labeled CEP164$^{1–588}$ and TTBK2$^{1074E}$ with fluorescence dyes Cy5 or Cy3, respectively. Under the fluorescence microscope, we confirmed that the Cy3-TTBK2$^{1074E}$ and Cy5-CEP164$^{1–588}$ were localized in the same condensates (Figure 3G). The number of condensates increased when the protein concentration was raised (Figures S4D and S4E). By monitoring the samples' optical density at 600 nm, the turbidity of the samples increased with protein concentration, agreeing that the interaction of CEP164 and TTBK2 promotes condensate formation (Figure 3H).

The interaction between CEP164 and TTBK2 has been reported to depend on the presence of the WW domain (residues 56–89) within CEP164 and the proline-rich region of TTBK2.[11,21,22] To explore the involvement of the WW domain in this interaction, we generated two CEP164 mutants. The first mutant, CEP164$^{110–588}$, had residues 1–109 (containing the entire WW domain) deleted (Figures 3I and S5A). The second mutant, CEP164$^{1–588_2Y/A}$, carried tyrosine-to-alanine substitution at positions 73 and 74, which are known to disrupt CEP164/TTBK2 interactions (Figures 3I and S5B).[22] The *in vitro* assay shows that CEP164$^{1–588}$, CEP164$^{110–588}$, and CEP164$^{1–588_2Y/A}$ all exhibited similar condensation behavior, suggesting that the WW domain is not involved in CEP164/TTBK2-mediated condensate formation (Figures 3J and S5C–S5E).

## Electrostatic force drives TTBK2 and CEP164 phase separation

The sequence analysis shows that the regions of TTBK2 and CEP164 we studied accumulate with positively or negatively charged residues (Figure 4A). This trait of charge distribution is evolutionarily conserved (Figure 4A shows representative species; see Data S1 and S2 for all orthologs in the database). The multiple sequence alignment approach has limitations in capturing conserved residues among IDRs due to the lack of structural constraints, but their important physiochemical properties are often preserved through evolution.[46,47] Accordingly, the conserved physical properties in the amino acid composition hint that the electrostatic force may contribute to their condensation. To test whether the electrostatic force drives CEP164/TTBK2 condensation, we added different concentrations of salt (NaCl) to the condensates. We observed a decrease in condensation levels as the salt concentration increased, with complete dissolution of condensates occurring at concentrations above 700 mM (in a 1:1 ratio of 20 μM protein each), suggesting a dominant charge interaction between CEP164 and TTBK2 (Figures 4B and 4C). On the other hand, hydrophobicity plays little role in their condensation because adding 1,6-hexanediol, a common alcohol in disrupting hydrophobic-mediated phase separation,[48] to CEP164/TTBK2 condensates showed little effect (Figures S6A and S6B).

To examine whether the highly positively charged property of TTBK2 contributes to CEP164 and TTBK2 phase separation, we purified the recombinant TTBK2$^{1074E}$ protein with all 29 positively charged residues (lysine and arginine) replaced by glycine (TTBK2$^{1074E_29\text{-}KR/G}$), except those encompassed in the polyproline region (Figures 4D and S6C). We did not observe condensates even when the concentration of TTKB2$^{1074E_29\text{-}KR/G}$ was 5-fold excess to CEP164$^{1–588}$, further confirming that the electrostatic driving force contributes to the phase separation of CEP164 and TTBK2 (Figures 4E and 4F).

## The phase separation of CEP164 and TTBK2 is necessary for primary ciliogenesis

To investigate the role of TTBK2 and CEP164 phase separation at centrioles, we generated TTBK2 variants with altered charges in their C-terminal regions by substituting lysine with alanine (Figure 4D). These TTBK2 mutants were expressed in *TTBK2* knockout U2OS cells that expressed PACT-mCherry, a centrosome marker (Figure 5A). Immunostaining revealed that reducing the positive charges in TTBK2 led to decreased TTBK2 localization at the centrioles (Figures 5B and 5C), suggesting the electrostatic force is required for the recruitment of TTBK2 to DAs. Given that substituting just five positively charged residues within the TTBK2 C terminus (TTBK2$^{FL_5\text{-}KR/G}$)

**Figure 3. CEP164 and TTBK2 form condensates**

(A) GFP-CEP164 was expressed in U2OS cells and immunostaining was performed using antibodies as indicated, with DAPI used to label the nuclei. The magnified views on the right correspond to regions demarcated by boxes. Scale bars are as indicated.

(B) A schematic diagram shows different TTBK2 constructs tagged with FLAG and HA (FH). The percentage of positive signals for each TTBK2 mutant at the centrioles is shown.

(C) Co-transfection of Myc-CEP164 was carried out with various FH-TTBK2 constructs in *TTBK2* knockout U2OS cells. Staining for Myc and HA was performed to identify the minimal TTBK2 fragment detected in CEP164 condensates. Regions within the marked boxes are magnified and shown on the right. Scale bars are as indicated.

(D) The proportion of positive TTBK2 signals present within CEP164 condensates was quantified. A minimum of 100 cells from a total of $n = 3$ independent experiments were analyzed. Error bars represent the mean ± SEM. n.s., not significant, and $^{***}p < 0.001$ by one-way ANOVA.

(E) FH-TTBK2$^{1074E}$ was co-expressed with Myc-CEP164$^{1–588}$ in 293T cells. Cell lysate was subjected to anti-FLAG immunoprecipitation followed by western blot analysis.

(F) Bright-field images of 20 μM CEP164$^{1–588}$, 20 μM TTBK2$^{1074E}$, or their combination *in vitro* in phosphate buffer. Experiments were performed at least three times for each condition. The represented images are shown.

(G) Cy3-labeled TTBK2$^{1074E}$ exhibited localization within the droplets along with Cy5-labeled CEP164$^{1–588}$. The magnified views on the right show the region outlined by the box. Scale bars are as indicated.

(H) Different concentrations of CEP164$^{1–588}$ and TTBK2$^{1074E}$ proteins were subjected to *in vitro* incubation in phosphate buffer and subsequently quantified using $OD_{600}$ measurements.

(I) A schematic diagram shows different CEP164 constructs.

(J) Bright-field images of 20 μM CEP164$^{110–588}$, 20 μM TTBK2$^{1074E}$, or their combination *in vitro* in phosphate buffer. Experiments were performed at least three times for each condition. The represented images are shown. Scale bar, 10 μm.

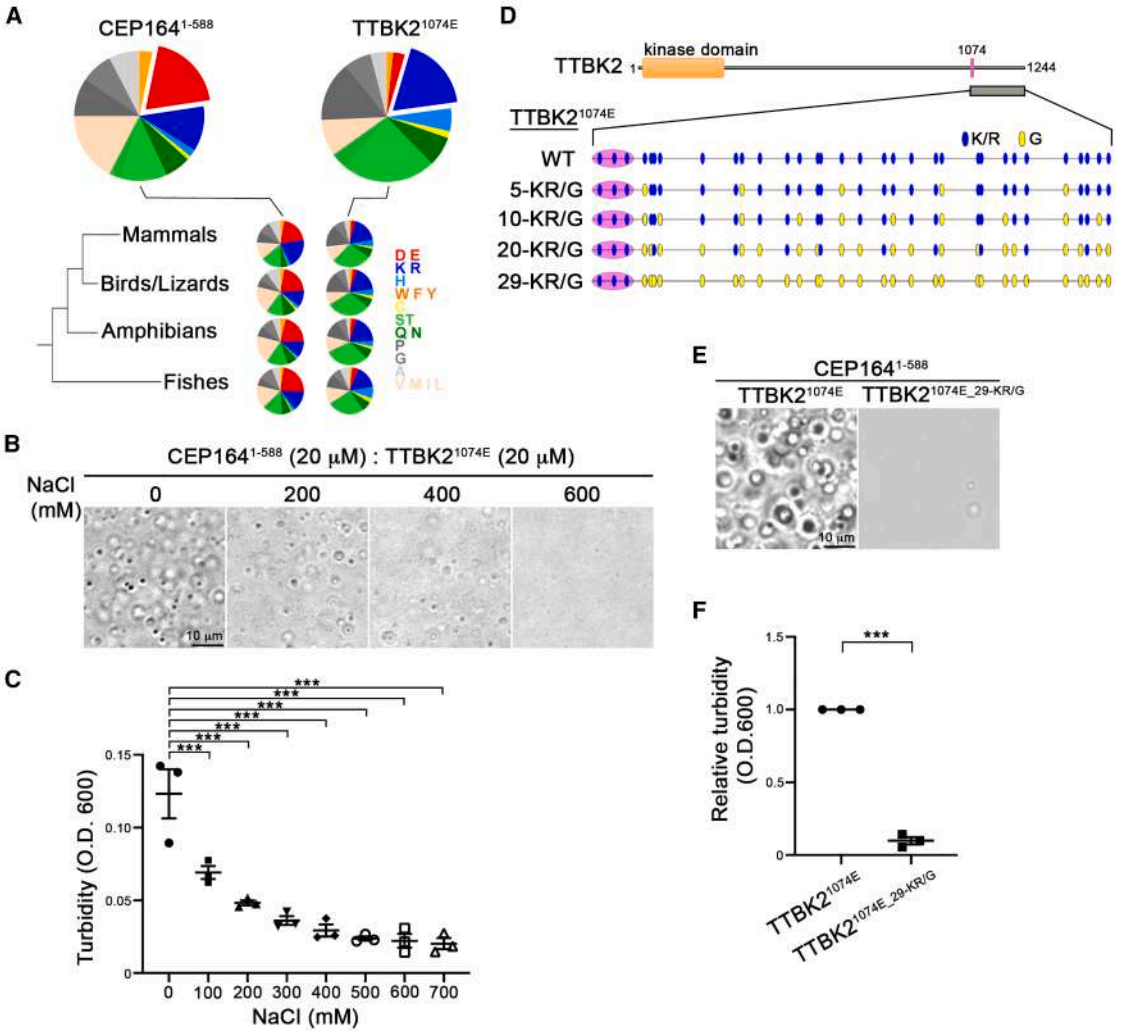


**Figure 4. CEP164 and TTBK2 form condensates via electrostatic interaction**

(A) Amino acid pie charts display the composition of CEP164$^{1–588}$ and TTBK2$^{1074E}$ sequences from several species.

(B) 20 μM CEP164$^{1–588}$ and 20 μM TTBK2$^{1074E}$ were incubated with varying concentrations of NaCl in phosphate buffer. Representative bright-field images are shown. Scale bar, 10 μm.

(C) The turbidity of the incubation solution was assessed using $OD_{600}$ measurements. The error bars represent the mean ± SD. ***$p < 0.001$ by one-way ANOVA from 3 independent experiments.

(D) A schematic diagram shows the assortment KR-to-G mutations in TTBK2$^{1074E}$ fragment. The magenta box indicates the proline-rich region of TTBK2, encompassing resides 1074–1089.

(E) 20 μM CEP164$^{1–588}$ was incubated with either 20 μM TTBK2$^{1074E}$ or 20 μM TTBK2$^{1074E_29\text{-}KR/G}$. Representative bright-field images are shown. Scale bar, 10 μm.

(F) The turbidity assay was conducted by measuring 20 μM CEP164$^{1–588}$ incubated with either 20 μM TTBK2$^{1074E}$ or 20 μM TTBK2$^{1074E_29\text{-}KR/G}$ in phosphate buffer. The error bars represent the mean ± SD. ***$p < 0.001$ by one-way ANOVA from 3 independent experiments.

significantly reduced its localization at the centrioles, we purified recombinant TTBK2$^{1074E_5\text{-}KR/G}$ and mixed it with CEP164$^{1–588}$. While the mixture of CEP164$^{1–588}$ and TTBK2$^{1074E}$ readily formed condensates, the mixture with TTBK2$^{1074E_5\text{-}KR/G}$ showed a reduction in condensate formation (Figures 5D and 5E), confirming that electrostatic force promotes CEP164/TTBK2 condensates. To further examine the role of CEP164/TTBK2 phase separation in ciliogenesis, we stably expressed TTBK2$^{FL}$ and TTBK2$^{FL_5\text{-}KR/G}$ in *TTBK2* knockout RPE1 cells (Figure 5F). Clonal isolation followed by western blot analysis confirmed the equal expression levels of TTBK2$^{FL}$ and TTBK2$^{FL_5\text{-}KR/G}$. Compared to TTBK2$^{FL}$, TTBK2$^{FL_5\text{-}KR/G}$ showed reduced intensity at the centrioles, further confirming that the positively charged residues located at TTBK2 C terminus play a critical role in its recruitment to DAs (Figures 5G and 5H). To assess the impact of this reduced recruitment on ciliogenesis, cells were serum starved for 2 days to induce cilia formation. CP110, a known suppressor for ciliogenesis,[49] is typically removed from the mother centrioles to enable axoneme extension. In

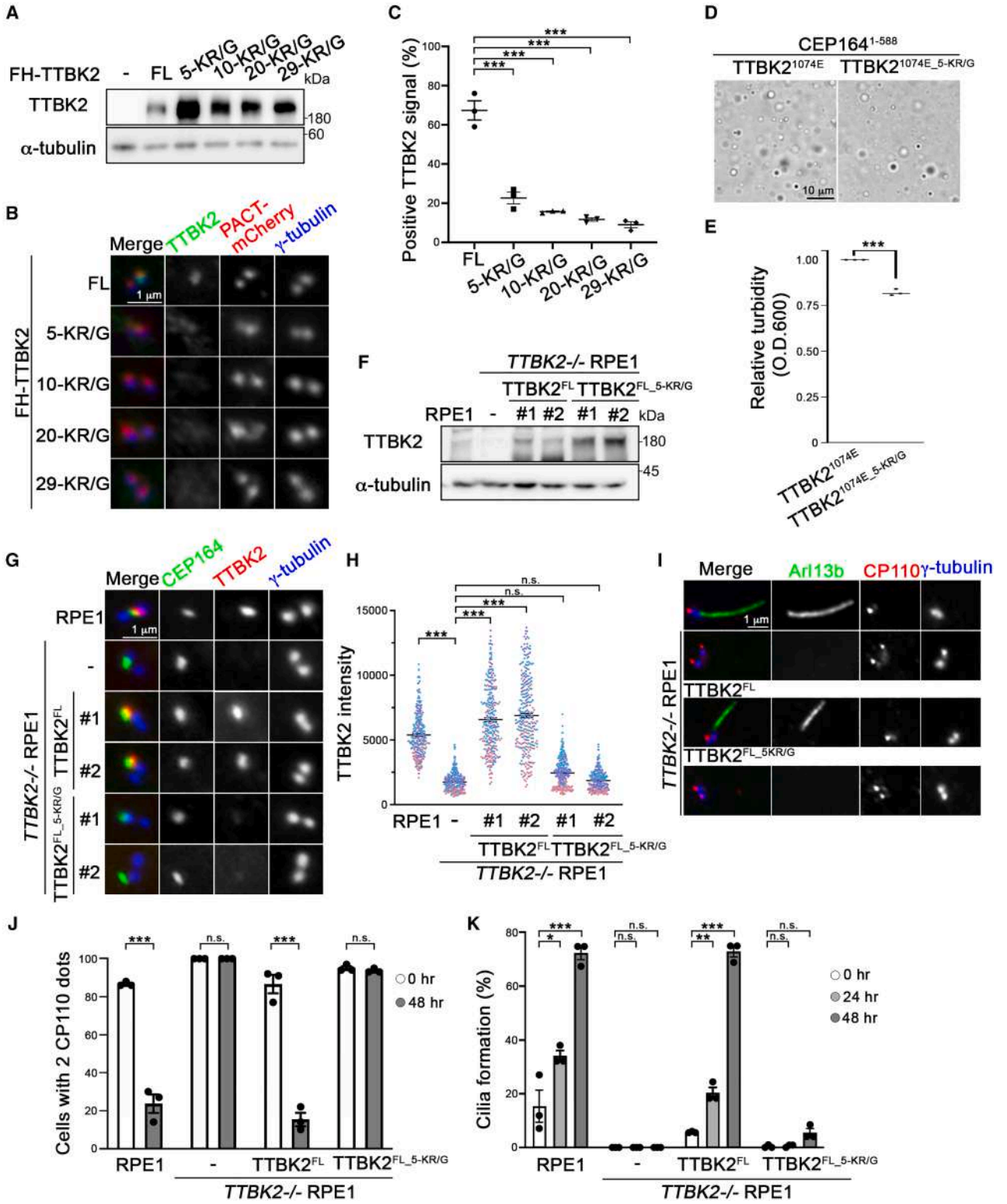


**Figure 5. The electrostatic interaction between CEP164 and TTBK2 is crucial for cilia formation**

(A) Different FH-TTBK2 KR-to-G mutants were expressed in *TTBK2* knockout U2OS cells. WB analyses were performed to assess TTBK2, with α-tubulin as the internal control.

(B) Immunostaining was carried out with using antibodies as indicated. Scale bar, 1 μm.

*(legend continued on next page)*

TTBK2$^{FL}$-expressing cells, serum starvation caused CP110 removal from the mother centrioles (Figures 5I and 5J). However, in cells expressing TTBK2$^{FL_5\text{-}KR/G}$, CP110 removal was impaired, with most cells displaying two distinct CP110 dots (Figures 5I and 5J), suggesting that the disruption of CEP164/TTBK2 phase separation inhibited primary cilia promotion. Using Arl13b as a ciliary marker further supported this, highlighting a notably diminished proportion of ciliated cells in TTBK2$^{FL_5\text{-}KR/G}$-expressing cells compared to TTBK2$^{FL}$-expressing cells (Figures 5I and 5K). Together, our findings demonstrate that CEP164/TTBK2 phase separation is essential for TTBK2 recruitment to DAs, thereby initiating primary ciliogenesis.

## DISCUSSION

The initiation of ciliogenesis requires the recruitment of TTBK2 to DAs via CEP164.[11,21,22] In this study, we uncover an additional layer of interaction between CEP164 and TTBK2, where CEP164's IDR drives the formation of dynamic condensates with TTBK2 through the phase separation mechanism mediated by electrostatic interactions. We also demonstrate that this phase-separation-driven interaction, together with the previously characterized binding between the WW domain of CEP164 and TTBK2 residues 1074–1089,[11,21,22] plays a cooperative role in facilitating the successful docking of TTBK2 to DAs, regulating the crucial initiation step of ciliogenesis (Figure S7). Our findings raise an intriguing question: what triggers the phase separation of CEP164 and TTBK2 at DAs? Given that electrostatic interactions are key to this process, one plausible mechanism involves post-translational modifications (PTMs), such as phosphorylation or dephosphorylation, which can alter the net charges of CEP164 or TTBK2, altering phase transition. Notably, CEP164 has been identified as a substrate of TTBK2 at the centrioles,[11,24] suggesting that PTMs during ciliogenesis could modify the electrostatic properties of their IDRs, promoting phase separation. Moreover, the microenvironment at the DAs could be significantly influenced by the presence of TTBK2, which serves as a phosphorylating agent for various downstream proteins associated with DAs, including CEP83 and MPP9.[23,24] This hypothesis does not exclude the possibility that other unknown enzymes are also recruited to the condensation to modify the microenvironment of DAs. The recruitment of these enzymes to the centrioles might, in turn, alter the charges on CEP164 or TTBK2. Identifying the potential modifiers is a promising avenue for future research.

Our study uncovers a two-step mechanism for the recruitment of TTBK2 to DAs, involving two distinct yet cooperative interactions with CEP164. The first step is the initial docking of TTBK2, mediated by the well-characterized interaction between the WW domain of CEP164 and the proline-rich region of TTBK2.[11,21,22] The second step, revealed in our current study, involves phase separation between CEP164 and TTBK2, which enhances the retention of TTBK2 at DAs. The requirement of phase separation is supported by our *in vitro* condensation assays using purified CEP164$^{110–588}$ or CEP164$^{1–588_2Y/A}$ incubated with TTBK2$^{1074E}$, independent of the interaction between the WW domain and TTBK2 (Figures 3J and S5C–S5E). However, the protein concentrations are lower in the cellular environment, and the initial docking between the WW and proline-rich domains is also required to ensure spatial specificity for the subsequent phase separation for the stable accumulation of TTBK2 at DAs.

Given the necessary roles played by both CEP164 and TTBK2 in ciliogenesis, it will be interesting to explore the potential involvement of CEP164/TTBK2 phase separation in diseases. For example, spinocerebellar ataxia type 11 (SCA11) is a neurodegenerative disorder characterized by gradual ataxia progression and cerebellar atrophy, and the mutations in the *TTBK2* gene are associated with SCA11.[50] These TTBK2 pathogenic variants generate either truncations or missense mutations.[51] Interestingly, a majority of missense variants in TTBK2 are reported to concentrate at its C terminus.[51] Since our findings indicate that the C terminus of TTBK2 is enriched with positive charges and is necessary for CEP164/TTBK2 phase separation, our results promote us to raise an interesting hypothesis that the disruption of CEP164/TTBK2 phase separation could potentially contribute to the development of SCA11. Further investigation of this hypothesis could illuminate the molecular underpinnings of SCA11 and potentially offer insights into therapeutic avenues for addressing ciliopathy-related disorders.

CEP164 is not the only DA protein characterized by the prevalence of IDRs and coiled-coil segments. In fact, all DA proteins

(C) The localization of different TTBK2 KR-to-G mutants at the centrioles was quantified. A minimum of 100 cells from a total of $n = 3$ independent experiments were analyzed. Error bars represent the mean ± SEM. $^{*}p < 0.05$ and $^{***}p < 0.001$ by one-way ANOVA.
(D) 20 μM CEP164$^{1–588}$ was incubated with either 20 μM TTBK2$^{1074E}$ or 20 μM TTBK2$^{1074E_5\text{-}KR/G}$ in phosphate buffer. Representative bright-field images are shown.
(E) The turbidity of the incubation solution was assessed using $OD_{600}$ measurements. The error bars represent the mean ± SD. $^{***}p < 0.001$ by one-way ANOVA.
(F) TTBK2$^{FL}$ and TTBK2$^{FL_5\text{-}KR/G}$ were stably expressed in *TTBK2* knockout RPE1 cells. WB analysis was performed to evaluate TTBK2 levels, with α-tubulin as the internal control.
(G) Immunostaining was conducted using anti-CEP164, anti-TTBK2, and anti-γ-tubulin antibodies. Scale bar, 1 μm.
(H) The intensity of TTBK2 at the centriole was quantified. At least 100 cells were analyzed for each independent experiment. Error bars represent mean ± SEM. $n = 3$.
(I) RPE1 cells were serum starved for 2 days to induce cilia formation. Immunostaining was performed using anti-Arl13b, anti-CP110, and anti-γ-tubulin antibodies. Representative images are shown. Scale bar, 1 μm.
(J) The positive CP100 signal at the centrioles was quantified in 2 day serum-starved RPE1 cells. At least 100 cells were analyzed for each independent experiment. Error bars represent mean ± SEM. $n = 3$.
(K) Cells were serum starved to induce cilia formation. The proportion of ciliated cells was quantified. At least 100 cells were analyzed for each independent experiment. Error bars represent mean ± SEM. $n = 3$.
In (H), (J), and (K), n.s., not significant, $^{*}p < 0.05$, $^{**}p < 0.01$, and $^{***}p < 0.001$ by Student's t test.

reveal a consistent trend of structural disorder and pronounced coiled-coil propensities (Figure S8). The coiled-coil interaction is also a well-documented "sticker" for multivalently crosslinking biomolecular condensation.[52,53] It would be intriguing to explore whether the other DA proteins share the capacity for undergoing phase separation within the cellular milieu. The dynamic properties of DA proteins would provide insights into how such a stable appendage can be regulated efficiently in between the flexible disordered structure and stable coiled-coil twisters upon the response to the signals of ciliogenesis. Understanding the mechanistic properties also offers potential therapeutic strategies for treating ciliopathies via targeting the phase separation mechanism, as has been proposed for treating neurodegenerative diseases[54] and RNA therapeutics.[55] Our study shows the first example of such a mechanism in the framework of ciliogenesis, offering a promising guide for future investigations.

### Limitations of the study

We generated two CEP164 mutants (CEP164$^{110–588}$ and CEP164$^{1–588_2Y/A}$) to disrupt the previously known CEP164/TTBK2 interaction. Neither mutant impaired phase separation with TTBK2 (Figures 3J and S5). However, the reciprocal experiment, i.e., removing the proline-rich region of TTBK2, was not achievable because of technical challenges associated with expressing and purifying related constructs. Deleting the proline-rich region (TTBK2$^{1085E}$) causes a dramatic reduction in protein expression, with only faint expression detectable by western blot (Figure S9A). Substitution of the six prolines (within residues 1074–1084) with glycine residues (TTBK2$^{1074E_6P/G}$) further exacerbated this effect, resulting in undetectable expression (Figure S9A). Additional constructs, including TTBK2$^{1084E}$ and TTBK2$^{1086E}$, also failed to yield detectable protein. Our findings indicate that this proline-rich region might be critical for protein stability. To address this, we fused a SUMO tag to TTBK2$^{1085E}$ to improve expression levels (Figure S9A). However, the fusion protein remained highly unstable and prone to degradation (Figure S9B). Despite these technical limitations, our findings support that the 1074–1085 proline-rich region is not essential for CEP164-TTBK2 phase separation *in vitro*, as CEP164 lacking its WW domain could still undergo phase separation with TTBK2$^{1074E}$ (Figures 3J and S5). This indicates that phase separation between CEP164 and TTBK2 can occur independently of the WW domain/proline-rich region interaction *in vitro*.

## RESOURCE AVAILABILITY

### Lead contact

Further information and requests for resources and reagents should be directed to and will be fulfilled by the lead contact, Won-Jing Wang (wangwj@nycu.edu.tw).

### Materials availability

All reagents generated during this study are available from the lead contact with a completed materials transfer agreement.

### Data and code availability

Data are available upon request to the lead contact.

This study does not report original code.

Scripts used to analyze the phylogenetic relationships of CEP164 and TTBK2 orthologs are available upon request from Jie-rong Huang (jierongh@nycu.edu.tw).

## ACKNOWLEDGMENTS

This work was supported by the National Science and Technology Council of Taiwan (NSTC) (110-2628-B-A49A-508, 110-2326-B-A49A-503-MY3, 112-2628-B-A49-009-MY3, and 113-2320-B-A49-018-MY3 to W.-J.W.; 110-2113-M-A49A-504-MY3 and 113-2113-M-A49-031-MY3 to J.-r.H.; 113-2628-B-007-003, and 114-2740-B-007-001 to Y.-C.L.; and 113-2628-E-002-014 to T.T.Y.), the Yen Tjing Ling Medical Foundation (CI-110-16 and CI-111-19 to J.-r.H.), the Higher Education Sprout Project by the Ministry of Education (MOE) in Taiwan to W.-J.W. and J.-r.H., and the NYCU-FRMH Joint Research Program (112DN01 and 114DN03 to W.-J.W.). We thank Yu-Chen Chen for handling some protein purification.

## AUTHOR CONTRIBUTIONS

P.-C.C., J.-r.H., and W.-J.W. designed the experiments and analyzed the data. P.-C.C. performed most of the experiments. Y.-C.H., Y.L., and Y.-H.L. purified the recombinant proteins and performed the *in vitro* phase separation experiments. S.-R.H. contributed to the FRAP experiments. I.-H.L. generated TTBK2 mutants. Y.-J.B.C. and T.T.Y. contributed to Ex-dSTORM. P.-C.C. wrote the initial draft of the manuscript. Y.-C.L., T.T.Y., J.-r.H., and W.-J.W. discussed the paper. J.-r.H. and W.-J.W. wrote and edited the final manuscript with comments from all authors.

## DECLARATION OF INTERESTS

The authors declare that they have no competing financial interests.

## STAR★METHODS

Detailed methods are provided in the online version of this paper and include the following:

- KEY RESOURCES TABLE
- EXPERIMENTAL MODEL AND STUDY PARTICIPANT DETAILS
  - Cell lines and transfection
- METHOD DETAILS
  - Cloning
  - Lentivirus production and infection
  - Generation of gene-editing cells
  - Immunofluorescence and image quantification
  - Fluorescence recovery after photo bleaching (FRAP)
  - Western blotting
  - Antibodies
  - Protein sequence analysis
  - Protein purification
  - Microscopy for *in vitro* assay
  - Turbidity assay
  - Super-resolution expansion
- QUANTIFICATION AND STATISTICAL ANALYSIS

## SUPPLEMENTAL INFORMATION

Supplemental information can be found online at https://doi.org/10.1016/j.celrep.2025.115810.

Received: November 13, 2023
Revised: February 7, 2025
Accepted: May 19, 2025
Published: June 7, 2025

## REFERENCES


1. Christensen, S.T., Pedersen, L.B., Schneider, L., and Satir, P. (2007). Sensory cilia and integration of signal transduction in human health and disease. Traffic *8*, 97–109. https://doi.org/10.1111/j.1600-0854.2006.00516.x.
2. Garcia-Gonzalo, F.R., Phua, S.C., Roberson, E.C., Garcia, G., Abedin, M., Schurmans, S., Inoue, T., and Reiter, J.F. (2015). Phosphoinositides Regulate Ciliary Protein Trafficking to Modulate Hedgehog Signaling. Dev. Cell *34*, 400–409. https://doi.org/10.1016/j.devcel.2015.08.001.
3. Fliegauf, M., Benzing, T., and Omran, H. (2007). When cilia go bad: cilia defects and ciliopathies. Nat. Rev. Mol. Cell Biol. *8*, 880–893. https://doi.org/10.1038/nrm2278.
4. Breslow, D.K., and Holland, A.J. (2019). Mechanism and Regulation of Centriole and Cilium Biogenesis. Annu. Rev. Biochem. *88*, 691–724. https://doi.org/10.1146/annurev-biochem-013118-111153.
5. Carvalho-Santos, Z., Azimzadeh, J., Pereira-Leal, J.B., and Bettencourt-Dias, M. (2011). Evolution: Tracing the origins of centrioles, cilia, and flagella. J. Cell Biol. *194*, 165–175. https://doi.org/10.1083/jcb.201011152.
6. Gilula, N.B., and Satir, P. (1972). The ciliary necklace. A ciliary membrane specialization. J. Cell Biol. *53*, 494–509. https://doi.org/10.1083/jcb.53.2.494.
7. Reiter, J.F., Blacque, O.E., and Leroux, M.R. (2012). The base of the cilium: roles for transition fibres and the transition zone in ciliary formation, maintenance and compartmentalization. EMBO Rep. *13*, 608–618. https://doi.org/10.1038/embor.2012.73.
8. Sorokin, S. (1962). Centrioles and the formation of rudimentary cilia by fibroblasts and smooth muscle cells. J. Cell Biol. *15*, 363–377. https://doi.org/10.1083/jcb.15.2.363.
9. Streubel, J.M.S., and Pereira, G. (2023). Control of centrosome distal appendages assembly and disassembly. Cells Dev. *174*, 203839. https://doi.org/10.1016/j.cdev.2023.203839.
10. Tanos, B.E., Yang, H.J., Soni, R., Wang, W.J., Macaluso, F.P., Asara, J.M., and Tsou, M.F.B. (2013). Centriole distal appendages promote membrane docking, leading to cilia initiation. Genes Dev. *27*, 163–168. https://doi.org/10.1101/gad.207043.112.
11. Cajanek, L., and Nigg, E.A. (2014). Cep164 triggers ciliogenesis by recruiting Tau tubulin kinase 2 to the mother centriole. Proc. Natl. Acad. Sci. USA *111*, E2841–E2850. https://doi.org/10.1073/pnas.1401777111.
12. Graser, S., Stierhof, Y.D., Lavoie, S.B., Gassner, O.S., Lamla, S., Le Clech, M., and Nigg, E.A. (2007). Cep164, a novel centriole appendage protein required for primary cilium formation. J. Cell Biol. *179*, 321–330. https://doi.org/10.1083/jcb.200707181.
13. Joo, K., Kim, C.G., Lee, M.S., Moon, H.Y., Lee, S.H., Kim, M.J., Kweon, H.S., Park, W.Y., Kim, C.H., Gleeson, J.G., and Kim, J. (2013). CCDC41 is required for ciliary vesicle docking to the mother centriole. Proc. Natl. Acad. Sci. USA *110*, 5987–5992. https://doi.org/10.1073/pnas.1220927110.
14. Kurtulmus, B., Yuan, C., Schuy, J., Neuner, A., Hata, S., Kalamakis, G., Martin-Villalba, A., and Pereira, G. (2018). LRRC45 contributes to early steps of axoneme extension. J. Cell Sci. *131*, jcs223594. https://doi.org/10.1242/jcs.223594.
15. Sillibourne, J.E., Hurbain, I., Grand-Perret, T., Goud, B., Tran, P., and Bornens, M. (2013). Primary ciliogenesis requires the distal appendage component Cep123. Biol. Open *2*, 535–545. https://doi.org/10.1242/bio.20134457.
16. Ye, X., Zeng, H., Ning, G., Reiter, J.F., and Liu, A. (2014). C2cd3 is critical for centriolar distal appendage assembly and ciliary vesicle docking in mammals. Proc. Natl. Acad. Sci. USA *111*, 2164–2169. https://doi.org/10.1073/pnas.1318737111.
17. Bowler, M., Kong, D., Sun, S., Nanjundappa, R., Evans, L., Farmer, V., Holland, A., Mahjoub, M.R., Sui, H., and Loncarek, J. (2019). High-resolution characterization of centriole distal appendage morphology and dynamics by correlative STORM and electron microscopy. Nat. Commun. *10*, 993. https://doi.org/10.1038/s41467-018-08216-4.
18. Yang, T.T., Chong, W.M., Wang, W.J., Mazo, G., Tanos, B., Chen, Z., Tran, T.M.N., Chen, Y.D., Weng, R.R., Huang, C.E., et al. (2018). Super-resolution architecture of mammalian centriole distal appendages reveals distinct blade and matrix functional components. Nat. Commun. *9*, 2023. https://doi.org/10.1038/s41467-018-04469-1.
19. Jackson, P.K. (2012). TTBK2 kinase: linking primary cilia and cerebellar ataxias. Cell *151*, 697–699. https://doi.org/10.1016/j.cell.2012.10.027.
20. Goetz, S.C., Liem, K.F., Jr., and Anderson, K.V. (2012). The spinocerebellar ataxia-associated gene Tau tubulin kinase 2 controls the initiation of ciliogenesis. Cell *151*, 847–858. https://doi.org/10.1016/j.cell.2012.10.010.
21. Rosa, E.S.I., Bino, L., Johnson, C.M., Rutherford, T.J., Neuhaus, D., Andreeva, A., Cajanek, L., and van Breugel, M. (2022). Molecular mechanisms underlying the role of the centriolar CEP164-TTBK2 complex in ciliopathies. Structure *30*, 114–128 e119. https://doi.org/10.1016/j.str.2021.08.007.
22. Oda, T., Chiba, S., Nagai, T., and Mizuno, K. (2014). Binding to Cep164, but not EB1, is essential for centriolar localization of TTBK2 and its function in ciliogenesis. Genes Cells *19*, 927–940. https://doi.org/10.1111/gtc.12191.
23. Huang, N., Zhang, D., Li, F., Chai, P., Wang, S., Teng, J., and Chen, J. (2018). M-Phase Phosphoprotein 9 regulates ciliogenesis by modulating CP110-CEP97 complex localization at the mother centriole. Nat. Commun. *9*, 4511. https://doi.org/10.1038/s41467-018-06990-9.
24. Lo, C.H., Lin, I.H., Yang, T.T., Huang, Y.C., Tanos, B.E., Chou, P.C., Chang, C.W., Tsay, Y.G., Liao, J.C., and Wang, W.J. (2019). Phosphorylation of CEP83 by TTBK2 is necessary for cilia initiation. J. Cell Biol. *218*, 3489–3505. https://doi.org/10.1083/jcb.201811142.
25. Obradovic, Z., Peng, K., Vucetic, S., Radivojac, P., and Dunker, A.K. (2005). Exploiting heterogeneous sequence properties improves prediction of protein disorder. Proteins *61*, 176–182. https://doi.org/10.1002/prot.20735.
26. Mittag, T., and Pappu, R.V. (2022). A conceptual framework for understanding phase separation and addressing open questions and challenges. Mol. Cell *82*, 2201–2214. https://doi.org/10.1016/j.molcel.2022.05.018.
27. Su, Q., Mehta, S., and Zhang, J. (2021). Liquid-liquid phase separation: Orchestrating cell signaling through time and space. Mol. Cell *81*, 4137–4146. https://doi.org/10.1016/j.molcel.2021.09.010.
28. Boija, A., Klein, I.A., Sabari, B.R., Dall'Agnese, A., Coffey, E.L., Zamudio, A.V., Li, C.H., Shrinivas, K., Manteiga, J.C., Hannett, N.M., et al. (2018). Transcription Factors Activate Genes through the Phase-Separation Capacity of Their Activation Domains. Cell *175*, 1842–1855.e16. https://doi.org/10.1016/j.cell.2018.10.042.
29. Larson, A.G., Elnatan, D., Keenen, M.M., Trnka, M.J., Johnston, J.B., Burlingame, A.L., Agard, D.A., Redding, S., and Narlikar, G.J. (2017). Liquid droplet formation by HP1alpha suggests a role for phase separation in heterochromatin. Nature *547*, 236–240. https://doi.org/10.1038/nature22822.
30. Sabari, B.R., Dall'Agnese, A., Boija, A., Klein, I.A., Coffey, E.L., Shrinivas, K., Abraham, B.J., Hannett, N.M., Zamudio, A.V., Manteiga, J.C., et al. (2018). Coactivator condensation at super-enhancers links phase separation and gene control. Science *361*, eaar3958. https://doi.org/10.1126/science.aar3958.
31. Strom, A.R., Emelyanov, A.V., Mir, M., Fyodorov, D.V., Darzacq, X., and Karpen, G.H. (2017). Phase separation drives heterochromatin domain formation. Nature *547*, 241–245. https://doi.org/10.1038/nature22989.
32. Zamudio, A.V., Dall'Agnese, A., Henninger, J.E., Manteiga, J.C., Afeyan, L.K., Hannett, N.M., Coffey, E.L., Li, C.H., Oksuz, O., Sabari, B.R., et al. (2019). Mediator Condensates Localize Signaling Factors to Key Cell Identity Genes. Mol Cell *76*, 753–766 e756. https://doi.org/10.1016/j.molcel.2019.08.016.
33. Dao, T.P., Kolaitis, R.M., Kim, H.J., O'Donovan, K., Martyniak, B., Colicino, E., Hehnly, H., Taylor, J.P., and Castañeda, C.A. (2018). Ubiquitin

Modulates Liquid-Liquid Phase Separation of UBQLN2 via Disruption of Multivalent Interactions. Mol. Cell *69*, 965–978.e6. https://doi.org/10.1016/j.molcel.2018.02.004.

34. Yasuda, S., Tsuchiya, H., Kaiho, A., Guo, Q., Ikeuchi, K., Endo, A., Arai, N., Ohtake, F., Murata, S., Inada, T., et al. (2020). Stress- and ubiquitylation-dependent phase separation of the proteasome. Nature *578*, 296–300. https://doi.org/10.1038/s41586-020-1982-9.
35. Fujioka, Y., Alam, J.M., Noshiro, D., Mouri, K., Ando, T., Okada, Y., May, A. I., Knorr, R.L., Suzuki, K., Ohsumi, Y., and Noda, N.N. (2020). Phase separation organizes the site of autophagosome formation. Nature *578*, 301–305. https://doi.org/10.1038/s41586-020-1977-6.
36. Yamasaki, A., Alam, J.M., Noshiro, D., Hirata, E., Fujioka, Y., Suzuki, K., Ohsumi, Y., and Noda, N.N. (2020). Liquidity Is a Critical Determinant for Selective Autophagy of Protein Condensates. Mol. Cell *77*, 1163–1175. e9. https://doi.org/10.1016/j.molcel.2019.12.026.
37. Zhang, G., Wang, Z., Du, Z., and Zhang, H. (2018). mTOR Regulates Phase Separation of PGL Granules to Modulate Their Autophagic Degradation. Cell *174*, 1492–1506.e22. https://doi.org/10.1016/j.cell.2018.08.006.
38. Kilic, S., Lezaja, A., Gatti, M., Bianco, E., Michelena, J., Imhof, R., and Altmeyer, M. (2019). Phase separation of 53BP1 determines liquid-like behavior of DNA repair compartments. EMBO J. *38*, e101379. https://doi.org/10.15252/embj.2018101379.
39. Beutel, O., Maraspini, R., Pombo-Garcia, K., Martin-Lemaitre, C., and Honigmann, A. (2019). Phase Separation of Zonula Occludens Proteins Drives Formation of Tight Junctions. Cell *179*, 923–936 e911. https://doi.org/10.1016/j.cell.2019.10.011.
40. Schwayer, C., Shamipour, S., Pranjic-Ferscha, K., Schauer, A., Balda, M., Tada, M., Matter, K., and Heisenberg, C.P. (2019). Mechanosensation of Tight Junctions Depends on ZO-1 Phase Separation and Flow. Cell *179*, 937–952.e18. https://doi.org/10.1016/j.cell.2019.10.006.
41. Quiroz, F.G., Fiore, V.F., Levorse, J., Polak, L., Wong, E., Pasolli, H.A., and Fuchs, E. (2020). Liquid-liquid phase separation drives skin barrier formation. Science *367*, eaax9554. https://doi.org/10.1126/science.aax9554.
42. Woodruff, J.B., Ferreira Gomes, B., Widlund, P.O., Mahamid, J., Honigmann, A., and Hyman, A.A. (2017). The Centrosome Is a Selective Condensate that Nucleates Microtubules by Concentrating Tubulin. Cell *169*, 1066–1077.e10. https://doi.org/10.1016/j.cell.2017.05.028.
43. Park, J.E., Zhang, L., Bang, J.K., Andresson, T., DiMaio, F., and Lee, K.S. (2019). Phase separation of Polo-like kinase 4 by autoactivation and clustering drives centriole biogenesis. Nat. Commun. *10*, 4959. https://doi.org/10.1038/s41467-019-12619-2.
44. Yamamoto, S., and Kitagawa, D. (2019). Self-organization of Plk4 regulates symmetry breaking in centriole duplication. Nat. Commun. *10*, 1810. https://doi.org/10.1038/s41467-019-09847-x.
45. Hardenberg, M., Horvath, A., Ambrus, V., Fuxreiter, M., and Vendruscolo, M. (2020). Widespread occurrence of the droplet state of proteins in the human proteome. Proc. Natl. Acad. Sci. USA *117*, 33254–33262. https://doi.org/10.1073/pnas.2007670117.
46. Zarin, T., Strome, B., Peng, G., Pritišanac, I., Forman-Kay, J.D., and Moses, A.M. (2021). Identifying molecular features that are associated with biological function of intrinsically disordered protein regions. eLife *10*, e60220. https://doi.org/10.7554/eLife.60220.
47. Ho, W.L., Huang, H.C., and Huang, J.R. (2023). IFF: Identifying key residues in intrinsically disordered regions of proteins using machine learning. Protein Sci. *32*, e4739. https://doi.org/10.1002/pro.4739.
48. Wang, Z., Lou, J., and Zhang, H. (2022). Essence determines phenomenon: Assaying the material properties of biological condensates. J. Biol. Chem. *298*, 101782. https://doi.org/10.1016/j.jbc.2022.101782.
49. Yadav, S.P., Sharma, N.K., Liu, C., Dong, L., Li, T., and Swaroop, A. (2016). Centrosomal protein CP110 controls maturation of the mother centriole during cilia biogenesis. Development *143*, 1491–1501. https://doi.org/10.1242/dev.130120.
50. Bowie, E., Norris, R., Anderson, K.V., and Goetz, S.C. (2018). Spinocerebellar ataxia type 11-associated alleles of Ttbk2 dominantly interfere with ciliogenesis and cilium stability. PLoS Genet. *14*, e1007844. https://doi.org/10.1371/journal.pgen.1007844.
51. Felicio, D., and Santos, M. (2023). Spinocerebellar ataxia type 11 (SCA11): TTBK2 variants, functions and associated disease mechanisms. Cerebellum *23*, 678–687. https://doi.org/10.1007/s12311-023-01540-6.
52. Fang, X., Wang, L., Ishikawa, R., Li, Y., Fiedler, M., Liu, F., Calder, G., Rowan, B., Weigel, D., Li, P., and Dean, C. (2019). Arabidopsis FLL2 promotes liquid-liquid phase separation of polyadenylation complexes. Nature *569*, 265–269. https://doi.org/10.1038/s41586-019-1165-8.
53. Seim, I., Posey, A.E., Snead, W.T., Stormo, B.M., Klotsa, D., Pappu, R.V., and Gladfelter, A.S. (2022). Dilute phase oligomerization can oppose phase separation and modulate material properties of a ribonucleoprotein condensate. Proc. Natl. Acad. Sci. USA *119*, e2120799119. https://doi.org/10.1073/pnas.2120799119.
54. Hurtle, B.T., Xie, L., and Donnelly, C.J. (2023). Disrupting pathologic phase transitions in neurodegeneration. J. Clin. Investig. *133*, e168549. https://doi.org/10.1172/JCI168549.
55. Conti, B.A., and Oppikofer, M. (2022). Biomolecular condensates: new opportunities for drug discovery and RNA therapeutics. Trends Pharmacol. Sci. *43*, 820–837. https://doi.org/10.1016/j.tips.2022.07.001.
56. Hong, S.R., Wang, C.L., Huang, Y.S., Chang, Y.C., Chang, Y.C., Pusapati, G.V., Lin, C.Y., Hsu, N., Cheng, H.C., Chiang, Y.C., et al. (2018). Spatiotemporal manipulation of ciliary glutamylation reveals its roles in intraciliary trafficking and Hedgehog signaling. Nat. Commun. *9*, 1732. https://doi.org/10.1038/s41467-018-03952-z.
57. Lupas, A., Van Dyke, M., and Stock, J. (1991). Predicting coiled coils from protein sequences. Science *252*, 1162–1164. https://doi.org/10.1126/science.252.5009.1162.
58. Sigrist, C.J.A., Cerutti, L., de Castro, E., Langendijk-Genevaux, P.S., Bulliard, V., Bairoch, A., and Hulo, N. (2010). PROSITE, a protein domain database for functional characterization and annotation. Nucleic Acids Res. *38*, D161–D166. https://doi.org/10.1093/nar/gkp885.
59. Feng, X.H., Filvaroff, E.H., and Derynck, R. (1995). Transforming growth factor-beta (TGF-beta)-induced down-regulation of cyclin A expression requires a functional TGF-beta receptor complex. Characterization of chimeric and truncated type I and type II receptors. J. Biol. Chem. *270*, 24237–24245. https://doi.org/10.1074/jbc.270.41.24237.
60. Liu, G.Y., Chen, S.C., Lee, G.H., Shaiv, K., Chen, P.Y., Cheng, H., Hong, S. R., Yang, W.T., Huang, S.H., Chang, Y.C., et al. (2022). Precise control of microtubule disassembly in living cells. EMBO J. *41*, e110472. https://doi.org/10.15252/embj.2021110472.
61. Mali, P., Yang, L., Esvelt, K.M., Aach, J., Guell, M., DiCarlo, J.E., Norville, J.E., and Church, G.M. (2013). RNA-guided human genome engineering via Cas9. Science *339*, 823–826. https://doi.org/10.1126/science.1232033.
62. UniProt Consortium (2019). UniProt: a worldwide hub of protein knowledge. Nucleic Acids Res. *47*, D506–D515. https://doi.org/10.1093/nar/gky1049.
63. Altenhoff, A.M., Train, C.M., Gilbert, K.J., Mediratta, I., Mendes de Farias, T., Moi, D., Nevers, Y., Radoykova, H.S., Rossier, V., Warwick Vesztrocy, A., et al. (2021). OMA orthology in 2021: website overhaul, conserved isoforms, ancestral gene order and more. Nucleic Acids Res. *49*, D373–D379. https://doi.org/10.1093/nar/gkaa1007.
64. Sievers, F., Wilm, A., Dineen, D., Gibson, T.J., Karplus, K., Li, W., Lopez, R., McWilliam, H., Remmert, M., Söding, J., et al. (2011). Fast, scalable generation of high-quality protein multiple sequence alignments using Clustal Omega. Mol. Syst. Biol. *7*, 539. https://doi.org/10.1038/msb.2011.75.

65. Huerta-Cepas, J., Serra, F., and Bork, P. (2016). ETE 3: Reconstruction, Analysis, and Visualization of Phylogenomic Data. Mol. Biol. Evol. *33*, 1635–1638. https://doi.org/10.1093/molbev/msw046.

66. Alberti, S., Saha, S., Woodruff, J.B., Franzmann, T.M., Wang, J., and Hyman, A.A. (2018). A User's Guide for Phase Separation Assays with Purified Proteins. J. Mol. Biol. *430*, 4806–4820. https://doi.org/10.1016/j.jmb.2018.06.038.

67. Chang, T.J.B., Hsu, J.C.C., and Yang, T.T. (2023). Single-molecule localization microscopy reveals the ultrastructural constitution of distal appendages in expanded mammalian centrioles. Nat. Commun. *14*, 1688. https://doi.org/10.1038/s41467-023-37342-x.

## STAR★METHODS

### KEY RESOURCES TABLE

| REAGENT or RESOURCE | SOURCE | IDENTIFIER |
|---|---|---|
| Antibodies | | |
| Mouse anti-centrin (20H5) | Millipore | Cat# 04–1624; RRID:AB_10563501 |
| Rabbit anti-CEP164 | Novus Biologicals | Cat# 45330002; RRID:AB_10004904 |
| Goat anti-CEP164 | Santa Cruz Biotechnology | Cat# sc-240226; RRID:AB_10841981 |
| Mouse anti-CEP164 | Santa Cruz Biotechnology | Cat# sc-515403 |
| Mouse anti-HA | BioLegend | Cat# 901503; RRID:AB_2565005 |
| Mouse anti–γ-tubulin (Tu30) | Santa Cruz Biotechnology | Cat# sc-51715; RRID:AB_630410 |
| Mouse anti-Flag (M2) | Sigma-Aldrich | Cat# F3165; RRID:AB_259529 |
| Rabbit anti-TTBK2 | Atlas Antibodies | Cat# HPA018113; RRID:AB_1858421 |
| Rabbit anti-Myc | Cell Signaling Technology | Cat# 2278; RRID:AB_490778 |
| Mouse anti-Myc | Cell Signaling Technology | Cat# 2276; RRID:AB_331783 |
| Mouse anti–β-actin | Novus Biologicals | Cat# NB600-501; RRID:AB_343280 |
| Rabbit anti-CP110 | Proteintech | Cat# 12780-I-AP; RRID:AB_10638480 |
| Mouse anti-Arl13b | Abcam | Cat# ab136648; RRID:AB_3073658 |
| Rat anti-SCLT1 | | Tanos et al., 2013[10] |
| Chemicals, peptides, and recombinant proteins | | |
| DMEM medium | Thermo Fisher Scientific | 12800017 |
| DMEM medium/F12 | Thermo Fisher Scientific | 1240024 |
| T-Pro NTR II transfection reagents | T-Pro Biotechnology | JT97-N002M |
| Puromycin | Sigma-Aldrich | P8833 |
| Neomycin (G418) | Thermo Fisher Scientific | 10131027 |
| Cyanine3 NHS ester | Lumiprobe | 21020 |
| Cyanine5 NHS ester | Lumiprobe | 23020 |
| mPEG-Silane-5000 | Laysan Bio | 1626 |
| Experimental model: Cell lines | | |
| HEK293T | ATCC | Cat# CRL-3216; RRID:CVCL_0063 |
| 293FT | Thermo Fisher Scientific | Cat# R70007; RRID:CVCL_6911 |
| U2OS | ATCC | Cat# HTB-96; RRID:CVCL_0042 |
| RPE1 (hTERT-RPE1) | ATCC | Cat# CRL-4000; RRID:CVCL_4388 |
| Recombinant DNA | | |
| pRK5-CEP164$^{FL}$ -Myc | This study | N/A |
| pRcCMV-Myc-CEP164$^{FL}$ | This study | N/A |
| pEGFP-CEP164$^{FL}$ | This study | N/A |
| pCDNA3.1-CEP164 | This study | N/A |
| pCDNA3-FH-CEP164$^{FL}$ | This study | N/A |
| pET32a-His-CEP164$^{1-588}$ | This study | N/A |
| pET32a-His-CEP164$^{110-588}$ | This study | N/A |
| pET32a-His-CEP164$^{1-588_2YA}$ | This study | N/A |
| pCDNA3-FH-TTBK2$^{623E}$ | This study | N/A |
| pCDNA3-FH-TTBK2$^{967E}$ | This study | N/A |
| pCDNA3-FH-TTBK2$^{1074E}$ | This study | N/A |
| pCDNA3-FH-TTBK2$^{1085E}$ | This study | N/A |
| pET21-His-TTBK2$^{1074E}$ | This study | N/A |
| pET21-His-TTBK2$^{1074E_29\text{-}KR/G}$ | This study | N/A |
| pLAS.3W-FH-TTBK2$^{FL}$ | This study | N/A |

(*Continued on next page*)

*Continued*

| REAGENT or RESOURCE | SOURCE | IDENTIFIER |
|---|---|---|
| pLAS.3W-FH-TTBK2$^{KD}$ | This study | N/A |
| pLAS.3W-FH-TTBK2$^{FL_5\text{-}KR/G}$ | This study | N/A |
| pLAS.3W-FH-TTBK2 $^{FL\_10\text{-}KR/G}$ | This study | N/A |
| pLAS.3W-FH-TTBK2 $^{FL\_20\text{-}KR/G}$ | This study | N/A |
| pLAS.3W-FH-TTBK2 $^{FL\_29\text{-}KR/G}$ | This study | N/A |
| pBabe-puro-PACT-mCherry | This study | N/A |
| 5HT-mCherry | This study | Hong et al., 2018[56] |
| pgRNA_Cloning Vector | Addgene | RRID:Addgene_41824 |
| phCas9 | Addgene | RRID:Addgene_41815 |
| pgRNA-TTBK2 | This study | N/A |
| pgRNA-CEP164 | This study | N/A |
| **Software and algorithms** | | |
| PONDR | Obradovic et al.[25] | https://pondr.com/ |
| COILS | Lupas et al.[57] | https://npsa-prabi.ibcp.fr/cgi-bin/npsa_automat.pl?page=/NPSA/npsa_lupas.html |
| FuzDrop | Hardenberg et al.[45] | https://fuzdrop.bio.unipd.it/predictor |
| PROTSITE | Sigrist et al.[58] | https://prosite.expasy.org/ |
| ETE3 Toolkit | | https://etetoolkit.org/ |
| Clustral Omega | | https://www.ebi.ac.uk/jdispatcher/msa/clustalo |
| UniProt | | https://www.uniprot.org/ |
| OMA database | | https://omabrowser.org/oma/home/ |
| Photoshop | Adobe | |
| Prism 9 | GraphPad | |
| ZEN software | Zeiss | https://www.zeiss.com/microscopy/int/products/microscopesoftware/zen.html |
| ImageJ | National Institutes of Health | https://imagej.nih.gov/ij/index.html |
| **Other (primers for cloning)** | | |
| **Plasmid** | **Cloning primers** | |
| pCDNA3-FH-CEP164 | 5′CATGAATTCATGGCTGGACGACCCCTCCG-3′<br>5′TCTAGGCGGCCGCCTAGAAGCGATACACCTTCACTC-3′ | |
| pET21a-CEP164$^{1-588}$ | 5′GCCATCATATGATGGCTGGACGACCCCTCC-3′<br>5′CTCAGCGGCCGCTGAGAGCTGCTCTGGGGG-3′ | |
| pET21a-CEP164$^{110-588}$ | 5′ CATGAATTC ATG AAGAAGAAGAAAAAAAAA 3′<br>5′ CTCAGCGGCCGC TGAGAGCTGCTCTGGGGG-3′ | |
| pET21a-CEP164$^{1-588_2YA}$ | 5′ GCCATCATATGATGGCTGGACGACCCCTCCG-3′<br>5′GCCTGCTCGAGCAGGCCTTTGGACTGCTTGC-3′ | |
| pCDNA3-FH-TTBK2$^{1074E}$ | 5′GACTGCATATGCAGTCTAGAAAGAGCAAAA-3′<br>5′GATAGCTCGAGCTATCTGCTGAGTTTACTG-3′ | |
| pCDNA3-FH-TTBK2$^{1085E}$ | 5′AGGCCTCTCGAGAGGCCTGGAGTAGAAGCCAG-3′<br>5′GATAGCTCGAGCTATCTGCTGAGTTTACTG-3′ | |
| pET21-6His-TTBK2$^{1074E}$ | 5′AGGAAACTCGAGTTTCCTCGGCCACCACCAGG-3′<br>5′GATAGCTCGAGCTATCTGCTGAGTTTACTG-3′ | |
| pET21-6His-TTBK2$^{1074E_2\text{-}KR/G}$ | 5′AACATCATATGATGTTTCCTCGGCCACCACC-3′<br>5′GGTCTCGAGACCGCTGAGTCCACTGGCTG-3′ | |
| pLAS.3W-FH-TTBK2 $^{FL\_5\text{-}KR/G}$ | 5′CTGATGCTAGCGACTACAAGGACGACGAT-3′<br>5′GCAGAGTTTAAACTCTGCTGAGTTTACTGGC-3′ | |
| pLAS.3W-FH-TTBK2 $^{FL\_10\text{-}KR/G}$ | 5′TCCATGCTAGCATGGACTACAAGGACGACGAT-3′<br>5′GCAGAGTTTAAACTCTGCTGAGTCCACTGGC-3′ | |
| pLAS.3W-FH-TTBK2 $^{FL\_20\text{-}KR/G}$<br>pLAS.3W-FH-TTBK2 $^{FL\_29\text{-}KR/G}$ | 5′TCCATGCTAGCATGGACTACAAGGACGACGAT-3′<br>5′GCGGAGTTTAAACACCGCTGAGTCCACTGGC-3′ | |

(*Continued on next page*)

*Continued*

| REAGENT or RESOURCE | SOURCE | IDENTIFIER |
|---|---|---|
| Other (primers for genotyping) | | |
| *TTBK2* knockout U2OS cells | 5′-GATGCTGGCTGTTGACCAAA-3′<br>5′-TATACCCGGCTGACACCAGT-3′ | |
| *CEP164* knockout U2OS cells | 5′-CTGGGTGATTGATAACCATTGGG-3′<br>5′-CGCAAATGA AGCTCCTGACTCAGT-3′ | |
| *GFP-CEP164* U2OS cells | 5′-GAGCCTGTGAGCCTTGAGTT-3′<br>5′-ATGGCCGACAAGCAGAAGAA-3′<br>5′-CCACAGGCCTCTTCACAGAC-3′ | |
| Other (primers for mutagenesis) | | |
| $CEP164^{2Y/A}$ | 5′ACAGGTGACATTGCCGCCTTCAACTTCGCCAACGGGCAGT-3′<br>5′GGCGAAGTTGAAGGCGGCAATGTCACCTGTGATGTCCTGG-3′ | |

## EXPERIMENTAL MODEL AND STUDY PARTICIPANT DETAILS

### Cell lines and transfection

HEK293T, 293FT, and U2OS were maintained in DMEM medium, while RPE1 were cultured in DMEM/F-12 (1:1) medium. All mediums were supplemented with 10% fetal bovine serum (FBS) and 1% penicillin-streptomycin. Cells were cultured at 37°C with 5% $CO_2$. For transient transfection, $1.2 \times 10^5$ U2OS cells were seeded in a 12-well plate and allowed to adhere for 6–8 h. Transfection was performed using 1.5 μg of DNA and 3 μL T-Pro NTR II transfection reagents (JT97-N002M, T-Pro Biotechnology). Transfected cells were subsequently processed for western blotting or immunofluorescence analysis.

## METHOD DETAILS

### Cloning

Full-length CEP164 ($CEP164^{FL}$) cDNA was amplified from pRcCMV $CEP164$[12] via PCR and inserted into pRK5M vector,[59] which contains a C-terminal Myc epitope tag. $CEP164^{FL}$ was also cloned into the pCDNA3.1 vector and into a modified version of pCDNA3.1 containing N-terminal Flag and HA tags (referred to as pCDNA3-FH). For the expression of TTBK2 truncations, specific fragments of the TTBK2 were PCR amplified and cloned into pCDNA3-FH vector. Charge variants of TTBK2 with were generated by gene synthesis. Mutants of FH-TTBK2 were then cloned into pLAS-3W-puro lentiviral vector. To express recombinant proteins, DNA fragments encoding $CEP164^{1-588}$, $CEP164^{110-588}$ and $TTBK2^{1074E}$ were PCR amplified and cloned into bacterial expression vectors, either pET32a vector (+) (69015; Novagen) or pET21a (+). Site-directed mutagenesis was carried out to generate the $CEP164^{1-588\_2Y/A}$ mutant. To label the centrosome, we constructed a pbabe-puro-PACT-mCherry plasmid. The PACT-mCherry fragment was PCR-amplified from pPACT-CFP-FRB plasmid[60] and cloned into the pBabe-puro retrovial vector.

### Lentivirus production and infection

Approximately $3 \times 10^5$ 293FT cells were plated on a 60-well plate. The transfection was performed using T-Pro NTR II transfection reagents with the following plasmids: 1.5 μg pCMV-VSV-G, 2.5 μg pCMV-gag-pol, and 3 μg pLAS-3W-based constructs. The supernatant containing viral particles was collected after 48 h. To ensure purity, the virus-containing medium was filtered through a 0.45-μm filter. For the infection of U2OS and RPE1 cells, approximately $5 \times 10^5$ cells were seeded onto a 60-mm plate and allowed to grow overnight before incubating with viral stock. Two days after infection, cells were selected and maintained in the culture medium with 2 μg/mL puromycin (P8833, Sigma-Aldrich).

### Generation of gene-editing cells

Knockout cells were generated through co-expression of the Cas9 protein with indicated gRNAs, which are available from the Addgene (http://www.addgene.org/crispr/church/).[61] The targeted DNA sequences were cloned into the gRNA vector (Addgene, 41824) via the Gibson assembly method. The specific targeting sequence for *TTBK2* and *CEP164* genes are 5′-GAAAATGTT GCACTGAAGG-3’ (exon3 of *TTBK2*) and 5′-GCTGTTGGCAAAGGGCGACA-3’ (exon9 of *CEP164*). For GFP insertion at the N terminus of CEP164, the CEP164 gRNA were co-expressed with donor DNA that contained GFP cDNA in U2OS cells. The targeting DNA sequence for generating GFP-CEP164 is 5′- GAGCCCAGATGAGTCATGGC- 3’. Gene-editing cells were obtained by clonal propagation, starting from a single cell. Genotyping of these cells was carried out using primers listed in the key resources table.

### Immunofluorescence and image quantification

Cells were grown on 0.1 mg/mL poly-L-lysine–coated coverslips and fixed with cold methanol at −20°C for 15 min. Cells were incubated in the blocking buffer that contained 3% bovine serum albumin (wt/vol) and 0.1% Triton X-100 in PBS for 30 min at room temperature (RT). Primary antibodies were all diluted in the blocking buffer and incubated for 2 h at RT. Alexa Fluor 488-, 594-, or 680-conjugated secondary antibodies were 500x dilution (Molecular Probes) and incubated for 1 h at RT. Coverslips were mounted on the slides with mounting medium (ProLong Gold Antifade; Thermo Fisher Scientific). Fluorescent images were obtained using an upright microscope (Axio Imager M2 ApoTome2 system; Carl Zeiss) with a Plan-NEOFLUAR 63×oilimmersion objective (1.3 NA) and an Axiocam 702 mono charge-coupled device camera. Images were acquired and processed by ZEN software (Carl Zeiss) or ImageJ software (National Institutes of Health).

ZEN software was used to quantify staining signals at the centrioles. First, a consistent circular region (0.392 $\mu m^2$) was drawn around each centriole, with identical settings applied uniformly across all centrioles. Equivalent-sized circular regions were also delineated in the cytosol to serve as control regions. Results were expressed as means ± SEM. All the quantifications were conducted across a minimum of three independent experiments.

### Fluorescence recovery after photo bleaching (FRAP)

FRAP experiments in cells were carried out with a Nikon A1 confocal system (Nikon) and ×100 oil objective (Nikon). Before bleaching, three sequential images were taken to obtain a baseline of fluorescence intensity of GFP–CEP164. Fluorescence recovery of GFP-CEP164 was monitored for 10 min, and each image was taken for 10 s. The U2OS cells expressing GFP–CEP164 condensates were photobleached by 488 nm laser. The fluorescence intensity of GFP–CEP164 was measured with Nikon element AR software (Nikon). For monitor GFP-CEP164 condensates at the centrosome, PACT-mCherry (centrosome marker) was co-expressed with GFP-CEP164 to label the centrosomes.

### Western blotting

Cells were lysed in 1x RIPA lysis buffer (1% NP40, 10% SDS, 0.5% SDOC, 150 mM NaCl, 50 mM Tris-HCl at pH 8) and mixed with protease inhibitor (Roche, 4693132001). Cell debris were removed by centrifugation at 12,500x g for 15 min at 4°C. Equal amounts of proteins was mixed with SDS sample buffer, boiled at 95°C for 5 min, and separated by SDS-PAGE. Proteins were subsequently transferred from the gel to a polyvinylidene fluoride (PDVF) membrane (0.45 μm Hybond P, GE Healthcare). Membranes were blocked in 5% non-fat milk suspended in Tris-buffered saline supplemented with 0.1% Tween 20 (TBS-T) for 1 h, followed by incubation overnight at 4°C with primary with primary antibodies in TBS-T. Membranes were washed three times with TBS-T and incubated with HRP-conjugated anti-mouse or anti-rabbit secondary antibodies for 1 h at RT (Jackson ImmunoResearch). After washing three times with TBS-T, proteins were visualized with ECL Western blotting substrate.

### Antibodies

Antibodies used in this study include Rabbit anti-CEP164 (Immunofluorescence [IF] 1:200,000; 45330002; Novus Biologicals), Goat anti-CEP164 (IF 1:250; sc-240226; Santa Cruz), Mouse anti-CEP164 (IF 1:1000; sc-515403; Santa Cruz), Mouse anti-HA (IF 1:1,000; Western blot [WB] 1:1,000; 901503; BioLegend), Mouse anti-α-tubulin (WB 1:5,000; T6199; SigmaAldrich), Mouse anti–γ-tubulin (IF 1:250; sc-51715; Santa Cruz), mouse anti-centrin (IF 1:1,000; 04–1624; Millipore), Rabbit anti-TTBK2 (IF 1:2,500; WB 1:1000; HPA018113; Atlas Antibodies), Mouse anti-Myc (IF 1:1,000; 2278; Cell Signaling Technology), Mouse anti-β-actin (WB 1:5,000; NB600-501; Novus Biologicals), Mouse anti-pGlu-Tu (IF 1:3,000; 901501; AdpoGen), Mouse anti-SCLT1 (IF 1:1,000; 14875-1-AP; Proteintech), Rabbit anti-CP110 (IF 1:2,000; 12780-I-AP; Proteintech), and Mouse anti-Arl13b (IF 1:2,500; ab136648; Abcam).

### Protein sequence analysis

Primary protein sequences were obtained from UniProt.[62] Structural disorder, coiled-coil propensity, LLPS tendency, and structural motifs were predicted by PONDR,[25] COILS,[57] FuzDrop,[45] and PROTSITE[58] webservers, respectively. Orthologs of TTBK2 and CEP164 were identified via the Orthologous Matrix database[63] using the UniProt ID of the human proteins as input. Sequences of each ortholog were aligned using Clustral Omega.[64] Based on these alignments, residues corresponding to human TTBK2's 1074–1244 or human CEP164's 1–588 were retrieved, and the frequency of each amino acid type was computed using an in-house written Python script. Phylogenetic trees (Data S1 and S2) were generated using the ete3 toolkit based on the species retrieved from the aligned FASTA files.[65]

### Protein purification

For recombinant protein purification, constructs were transformed into *E. coli* BL21 (DE3) or Rosettas (DE3) (Novagen) cells. Transformed cells were cultured in LB medium at 37°C until the $O.D_{600}$ reached 0.6. Expression of the recombinant proteins was induced with a final concentration of 1 mM isopropyl-β-D-1-thiogalactopyranoside (IPTG) at 25°C overnight (~16 h). The cells were harvested and lysed in 20 mM Tris-HCl buffer with 300 mM NaCl and 10% glycerol at pH 8 (buffer A). After sonication and ultracentrifugation, the supernatant was filtered (0.45 μm) and loaded onto a nickel-charged immobilized metal affinity chromatography column (Qiagen). After being washed with 10x column volume (CV) of buffer A, the samples were washed with 1x CV of buffer A with extra 50 mM imidazole. The target samples were eluted with 5x CV of buffer B (buffer A with 500 mM imidazole).

For CEP164$^{1-588}$, CEP164$^{110-588}$, CEP164$^{1-588_2Y/A,}$ TTBK2$^{1074E_5\ kR/G}$, and TTBK2$^{1074E_29\ kR/G}$, the eluted protein samples were exchanged to the buffer C (20 mM Tris-HCl, pH 8.0) by a PD-10 column (GE Healthcare) and followed by an additional anion exchange purification (Macro-Prep High-Q Resin, BioRad). The purified protein was buffer exchanged to 20 mM sodium phosphate at pH 6.8. The concentrated sample (concentration was determined using the absorbance at 280 nm with a Nanodrop spectrometer) was frozen by liquid nitrogen and stored at −80°C before usage.

For TTBK2$^{1074E}$, the eluted sample was acidified using trifluoroacetic acid (down to pH ~3) and loaded onto a C4 reverse-phase column (Thermo Scientific Inc.). The sample was eluted in a gradient of acetonitrile using an HPLC system and then lyophilized. The lyophilized samples were stored in a dry cabinet until use. In the experiments, the sample powder was dissolved in 20 mM sodium phosphate buffer at pH 6.8, and the concentration was determined using the absorbance at 280 nm with a Nanodrop spectrometer.

### Microscopy for *in vitro* assay

To observe the condensates *in vitro*, protein samples were applied to mPEG-passivated slides following a standard protocol.[66] In short, glass slides for light microscopy were soaked in 2 M NaOH for 30 min and then cleaned with 2% Hellmanex (Ossila) in double-distilled $H_2O$ (dd $H_2O$). The cleaned slides were subjected to a microwave oven with warm water until the soap dispersed, followed by thorough rinsing with dd$H_2O$. Finally, the slides were sonicated in 70% ethanol for 10 min and then dried. The cleaned slides were soaked in a solution with 0.5% methoxy polyethylene glycol (mPEG) in ethanol containing 1% acetic acid at 70°C for 30 min. Excess mPEG was removed by immersing the slides in dd$H_2O$ and subjecting them to sonication. Following this step, the slides were rinsed with ddH2O and allowed to dry before being stored at a temperature of −20°C.

The bright-field micrographs were captured using an Olympus BX51 microscope equipped with a 40× long working distance objective lens. In the case of fluorescent microscopy, an eight-time molar excess of fluorescent dyes (Cy3-NHS or Cy5-NHS, Lumiprobe) was mixed with 2.5 mg lyophilized protein samples (TTBK2 or CEP164 fragments) in 0.1 M sodium phosphate at pH 8.3 for overnight at RT. The unbounded dyes were removed using a PD-10 column (GE Healthcare). The labeling efficiency was determined by the relative ratio between the extinction coefficients of the protein and the fluorescence dye (Cy5: 250,000 $M^{-1}$ $cm^{-1}$ at 650 nm; Cy3: 150,000 $M^{-1}$ $cm^{-1}$ at 554). Typically, the labeling efficiency was approximately 20%. The Cy3-or Cy5-labeled sample was aliquoted, flash-frozen, and stored at −80°C before usage. The microscope used for fluorescence images follows the method of immunofluorescence.

### Turbidity assay

The turbidity of the protein samples was quantified by measuring the light transmittance at 600 nm using a TECAN-Spark Plate Reader. Each protein sample (20 μL) was loaded into a 384-well plate. The turbidity values in all conditions were triplicated. The data are reported as mean ± SD.

### Super-resolution expansion

For Ex-dSTORM imaging, we followed the methods outlined in our previous work.[67] Initially, cells, fixed with cold methanol on coverslips, were subjected to treatment with an infusion solution composed of 1.4% formaldehyde and 2% acrylamide in PBS for a duration of 5 h at 37°C. Subsequently, the gelation solution, (19% (w/w) sodium acrylate, 10% (w/w) acrylamide, 0.1% (w/w) bisacrylamide, 0.5% (w/w) TEMED, and 0.5% (w/w) APS in PBS) was introduced to the infused cells in a chamber on ice for 1 min, followed by a 1-h incubation at 37°C. For denaturation, hydrogels were boiled at 95°C in the denaturation buffer (200mM SDS, 200mM NaCl, 50mM Tris-HCl, pH 9) for a duration of 90 min. Subsequently, the hydrogels underwent the first expansion in dd$H_2O$, followed by a PBS wash. Samples were then incubated in primary and secondary antibody solutions for 3 h at 37°C with gentle shaking. Additionally, a marker (ATP synthase, ab109867, Abcam) was labeled with Alexa Fluor 488 for drift correction. To immobilize ExM samples for dSTORM imaging, the expanded hydrogels were immersed in a freshly prepared re-embedding gel solution consisting of 10% (w/w) acrylamide (AA), 0.15% (w/w) BIS, 0.05% (w/w) TEMED, and 0.05% (w/w) APS in dd$H_2O$. This re-embedding gel solution was applied twice, with each incubation lasting for 25 min at room temperature and accompanied by gentle shaking. The polymerization process was carried out in a nitrogen-filled humidified chamber at 37°C for 1.5 h, followed by three washes in dd$H_2O$. For dSTORM imaging, the samples were immersed in an imaging buffer containing TN buffer, 10 mM mercaptoethylamine (MEA), and an oxygen-scavenging system comprising 10% glucose (G5767, Sigma-Aldrich), 0.5 mg $mL^{-1}$ glucose oxidase, and 40 μg $mL^{-1}$ catalase.

dSTORM imaging was performed on a home-built setup based on an inverted microscope (Eclipse Ti2-E, Nikon) and a laser merge module (ILE, Spectral Applied Research) with individual controllers for all light sources. For epi-illumination of samples, beams from a 637 nm laser (OBIS 637 LX 140 mW, Coherent), a 488 nm laser (OPSL 488 LX 150 mW, Coherent), and a 405 nm laser (OBIS 405 LX 100 mW, Coherent) were focused onto the back focal plane of an oil-immersing objective (100× 1.49, CFI Apo TIRF, Nikon). During the acquisition, the 637 nm laser was operated at an intensity of 2–5 kW/$cm^2$ and a weak 405 nm laser beam was introduced to convert fluorophores from a dark to a fluorescent state. The 488 nm laser was intermittently switched on every 800 frames for measuring lateral position drift. The fluorescent signal was cleaned through a quad-band filter (ZET405/488/561/640 mv2, Chroma), and then the signal was recorded on an electron-multiplying charge-coupled device (EMCCD) camera (iXon Life 888, Andor) with a pixel size of 83.5 nm. Typically, stream movies of 15,000–30,000 frames were acquired at a rate of 50 fps. Post-processing drift correction was conducted using a homemade code based on Labview, MATLAB, and ImageJ. Subsequently, individual molecule

was localized by MetaMorph Superresolution Module (Molecular Devices). The reconstructed Ex-dSTORM images were cleaned with the Gaussian filter of 1 pixel.

## QUANTIFICATION AND STATISTICAL ANALYSIS

GraphPad Prism 9 was used for data plotting and statistical analysis. Western blot band and images intensities were quantified using ImageJ. Results are presented as mean ± SEM or mean ± SD, as specified in the figure legends. The number of replicates (n) and the statistical tests used are also indicated in the figure legends. All quantifications are based on at least three independent experiments. Statistical significance is indicated as follows: n.s., not significant, *, $p < 0.05$, **, $p < 0.01$, ***, $p < 0.001$.